Title
Analytical investigation of high temperature 1kW solid oxide fuel cell system feasibility in methane hydrate recovery and deep ocean power generation

Journal
Applied Energy, 179(C)

ISSN
0306-2619

Authors
Azizi, Mohammad Ali
Brouwer, Jacob
Dunn-Rankin, Derek

Publication Date
2016-10-01

DOI
10.1016/j.apenergy.2016.06.119

Peer reviewed

Applied Energy 179 (2016) 909–928

Contents lists available at ScienceDirect

Applied Energy

journal homepage: www.elsevier.com/locate/apenergy

Analytical investigation of high temperature 1 kW solid oxide fuel cell system feasibility in methane hydrate recovery and deep ocean power generation

Mohammad Ali Azizi, Jacob Brouwer *, Derek Dunn-Rankin

National Fuel Cell Research Center, University of California, Irvine, CA 92697-3550, United States

HIGHLIGHTS

- A dynamic Solid Oxide Fuel Cell (SOFC) model was developed.
- Hydrate bed methane dissociation model was integrated with the SOFC model.
- SOFC operated steadily for 120 days at high pressure deep ocean environment.
- Burning some of the dissociated gas for SMR heat leads to more net methane produced.
- Higher SOFC fuel utilization produces higher integrated system efficiency.

ARTICLE INFO

Article history:
Received 8 April 2016
Received in revised form 6 June 2016
Accepted 25 June 2016
Available online 25 July 2016

Keywords:
SOFC
SMR
Hydrate dissociation
Thermal stimulation
Depressurization
Power generation

ABSTRACT

Methane hydrates are potential valuable energy resources. However, finding an efficient method for methane gas recovery from hydrate sediments is still a challenge. New challenges arise from increasing environmental protection. This is due in part to the technical difficulties involved in the efficient dissociation of methane hydrates at high pressures. In this study, a new approach is proposed to produce valuable products of: 1. *Net methane gas recovery from the methane hydrate sediment*, and 2. *Deep ocean power generation*. We have taken the first steps toward utilization of a fuel cell system in methane gas recovery from deep ocean hydrate sediments. An integrated high pressure and high temperature solid oxide fuel cell (SOFC) and steam methane reformer (SMR) system is analyzed for this application and the recoverable amount of methane from deep ocean sediments is measured. System analysis is accomplished for two major cases regarding system performance: 1. Energy for SMR is provided by the burning part of the methane gas dissociated from the hydrate sediment. 2. Energy for SMR is provided through heat exchange with fuel cell effluent gases. We found that the total production of methane gas is higher in the first case compared to the second case. The net power generated by the fuel cell system is estimated for all cases. The primary goal of this study is to evaluate the feasibility of integrated electrochemical devices to accomplish energy efficient dissociation of methane hydrate gases in deep ocean sediments. Concepts for use of electrochemical devices (e.g., high temperature fuel cells) for methane gas recovery from hydrates and efficient electricity production from the released gases are developed. The technical feasibility of these integrated systems for operation in hydrate reservoirs in deep ocean sediments was then evaluated using combined systems of thermodynamic and heat transfer equations, which are presented in detail.

1. Introduction

Currently, oil and natural gas are the world's primary energy resources. Methane hydrate deposits are abundant throughout the world and have been estimated to represent the greatest portion of the world's fossil energy reserves. Potential worldwide resources of methane hydrate have been estimated by different authors to be in the range of 3.1×10^{15} m^3 [1] to 7.6×10^{18} m^3 [2]. Detailed examinations showed that potential resources are in the order of 1.5×10^{16} m^3 [3,4]. Based on the NETL report, the amount of natural gas in the hydrate form is estimated to be as much as 2×10^{16} m^3 [5]. Estimates of hydrate natural gas in the

* Corresponding author.
E-mail address: jbrouwer@uci.edu (J. Brouwer).

http://dx.doi.org/10.1016/j.apenergy.2016.06.119
0306-2619/

North Slope of Alaska are in the order of 10^{13} ft^3, with additional 100's of trillions of cubic feet in other areas in the same region, and approximately 10^{15} ft^3 beneath the U.S. continental margin. Efficient extraction of these fuel resources could fulfill the world energy demand for many years. Despite the proved value of these hydrocarbon resources, no energy efficient technology for the recovery of these resources has yet been developed.

The main principles of hydrate plug formation and hydrate control were studied by Hammerschmidt in 1934 [6]. Methane hydrates are a crystal lattice, formed by water molecules in cages that contain methane molecules bonded to the water molecules by weak Van der Waals forces. Their properties and stability depend upon the values of equilibrium thermodynamic pressure and temperature. The basic cage of gas hydrate consists of a certain number of water and methane gas molecules (e.g. six water and one gas).

Potential environmental hazards of methane recovery from methane hydrate sediments regarding the green house gas production are well known. An immediate use of methane gas in power generating SOFC system could significantly increase the overall system efficiency by reducing the potential efficiency losses associated with the methane gas release in the distance between the methane hydrate bed and the on-shore power plant in case methane has to be delivered to the on-shore power plant. Today, most of the recovery systems that propose in-situ recovery mechanisms, have several risks associated with the methane gas release to ocean surface. In the proposed system of this study, these risks will be significantly mitigated by implementing sealed piping from the sediment to the reformer unit. In fact the authors believe that high efficiency of SOFC in power generation and immediate use of methane gas in SOFC reformer together can reduce these risks.

Several methods of hydrate prevention in technological systems have been developed up to now, and the most promising ones are: thermal stimulation, chemical injection/inhibition and depressurization. Several methods for hydrate formation prevention have been developed by Robinson and Ng [7]. Methane hydrates are not stable at sea level conditions, therefore in-situ energy efficient dissociation of gas hydrate and delivery of gas to the sea surface with the least amount of contamination are required. We have performed a system analysis in MATLAB/Simulink® to verify the feasibility of the integrated electrochemical devices (e.g., fuel cell system) and utilization in the hydrate reservoir in deep ocean sediments, using thermodynamic and heat transfer principles. Thermal stimulation and depressurization are the primary approaches included in this integrated system analysis. Proposed electrochemical devices, have high energy conversion efficiency and have the potential to improve the previous and current approaches of the methane hydrate dissociation in the field.

2. Methane hydrate properties

The temperature behavior of injection fluid and the heat capacity of hydrate sediments have been determined by Schoderbek [8]. Thermodynamic equations for the stability and solubility of methane hydrates have been derived by Tishchenko et al. and dissociation pressures have been calculated for various temperatures and salinities in the range of 273–293 K and 0–70 respectively [9]. The fugacity of methane gas and coefficients for the equation of state for the CH_4-CO_2-H_2O system in deep ocean sediments have been computed numerically. Numerical calculations of the dissociation pressure in the temperature range of 273–293 (K) and water salinity in the range of 0–70, have been accomplished by the research group of Duan et al. [10–12]. Hydrate saturation values for the Malik 2L-38 site at the arctic Mackenzie Delta have been reported to be 35–40% and at Northern Cascadia Margin confirmed to be 20–25% [13]. In one report by Colett et al., hydrate saturation in some cases exceeds 80% [14].

As provided in the literature, there are three main methods for gas hydrate recovery: 1. *Depressurization:* in which vertical wells are employed in the hydrate sediments. As a result of bringing the sediment pressure lower than the stable hydrate pressure, the gas hydrate dissociates. 2. *Thermal stimulation:* In this method, hydrate decomposition is induced by a thermal heat source operating at temperatures higher than the stable hydrate temperature. 3. *Chemical inhibitors*: this method involves displacement of methane hydrate equilibrium conditions beyond the hydrate stability zone through injecting a liquid inhibitor in the layer. It is well established that major parameters governing methane hydrate stability are *pressure*, *temperature* and *water salinity* [9]. Modeling gas hydrate dissociation requires the knowledge of thermodynamic properties of the hydrate so that one can determine the stability zone at the specific temperature and pressure. However, at equilibrium of the three phases in pure water, the dissociation pressure of gas hydrates is a function of temperature. Several experiments have been developed to express the relationships between the hydrate stability and thermodynamic parameters such as temperature and pressure and the local salinity (see, for example, Handa [15], Sloan [16]).

3. Thermal stimulation

The novel oxyfuel downhole steam generator (DSG) that has been developed by the PCI combustion group efficiently recovers methane gas from hydrate deposits while reducing the emissions. The proposed approach has the potential for carbon dioxide (CO_2) sequestration through CO_2/CH_4 exchange mechanism [17]. The results of this study, demonstrates that natural gas could be produced from hydrate sediment at an energy cost of approximately 15% of the heating value of methane gas. Parametrical study of methane hydrate dissociation in oceanic sediments, induced by thermal sources, has been accomplished for different values of permeability [18]. In that study, a semi-analytical model has been developed for the problem, based on the equilibrium in order to obtain further insight into the various parameters that can affect methane gas production. Permeability, porosity, and thermodynamic/transport properties of the system are among the parameters that have been thoroughly studied. Furthermore, the work proves that in contrast to previous studies of permafrost, the rate of hydrate dissociation depends upon the permeability of porous media in the case of oceanic sediments (i.e. less permeable sediment).

Velocity and the rate of hydrate dissociation are determined by Chatterjee et al. research group [19]. In that study, warm water has been used as a thermal source to stimulate hydrate dissociation. Total mass production of methane for various injection pressures and temperatures has been determined. In addition, it has been shown that despite the fact that the depressurization method has high energy efficiency regarding the net methane gas dissociation, it has a relatively low production rate compared to the warm water injection approach. Holder et al. have investigated feasibility of hydrate production from a thermodynamics point of view. This study shows that gas production is possible by thermally stimulating the hydrate rocks [20]. Upper and lower bounds of gas production and energy efficiency of the cyclic steam injection process have been determined by Bayles et al. in 1986 [21]. In one study, gas hydrate dissociation has been modeled as a moving boundary ablation process [22]. The model has been extended to thermal stimulation induced by hot water injection in the sediment [23]. Several experiments have been conducted by Ullerich et al. research group to calculate the rate of methane hydrate

dissociation under constant heat flux, generated by a thermal heat source [24]. A mathematical model for the dissociation process containing two movable phase transition boundaries (e.g., hydrate dissociation and ice melting fronts) has been proposed and solved using similarity transformations [25]. A numerical approach for gas hydrate recovery using magnetic thermal stimulation of hydrate sediment has been developed by Islam et al. [26]. In that study, vertical and horizontal wells have been deployed for the gas production. Methane hydrate dissociation using combusting heat source has been modeled by Castaldi et al. [27]. The results of that study have proved the possibility to reach the total energy efficiency of 90% for land-based reservoirs in the case where hydrate sediment loading is 20%. In a handful of studies, it has been suggested that thermal stimulation is the most attractive method for gas hydrate dissociation regarding energy efficiency [21,28]. One solution to the ablation problem of hydrate dissociation has been proposed in the Goodman et al. study, using the heat balance integral method with a second degree polynomial approximation for temperature profile [29]. Li et al. investigated the decomposition behaviors of methane hydrate in the porous media in the three-dimensional cubic hydrate simulator (CHS) using the huff and puff method with a single well with the different injection temperatures and different injection time [30]. In another study, they used the cubic hydrate simulator (CHS) to study the methane hydrate production behaviors in porous media by the thermal stimulation with a five-spot well system [31].

4. Depressurization

Torres et al., studied gas discharge from hydrate reservoir using a pressure difference approach at Northern Summit. They found that the gas discharge has a value of 6×10^4 mol/day [32]. Makogon et al. calculated the pressure drop that is necessary to initialize the hydrate dissociation process, as a function of sediment temperature [33]. In regions where the pressure is close to the dissociation pressure, it is reasonable to use depressurization as the main gas production approach. However, for the deposits that need very high pressure drop, such as *Black Ridge-1 (200 bar), Mexico-2 (250 bar), Costa Rica (260 bar), Peru-Chile-2 (305 bar), Nankai-2 (415 bar) and Peru-Chile-1 (430 bar)* it is not feasible to use depressurization, and other methods are suggested to be used [18]. A numerical model has been developed to simulate the isothermal process of gas production from Berea sandstone using depressurization. Experiments for hydrate dissociation have been developed by the Yousif et al. research group [34,35]. Goel et al. predicted the natural gas hydrate formation using depressurization approach involving decomposition kinetics in the hydrate dissociation process [36]. Li et al. studied behavior of methane hydrate in the sediment by depressurization in a novel pilot-scale hydrate simulator (PHS), a three-dimensional pressure vessel of 117.8 L [37]. In addition, the kinetic behaviors of methane hydrate dissociation under depressurization in porous media are investigated through experimental and numerical simulations [38]. Wang et al. have analytically investigated methane hydrate dissociation process by thermal stimulation, depressurization and depressurization in conjunction with thermal stimulation. The research suggests that the methane hydrate dissociation process would take a longer time than the thermal stimulation method. Also the authors concluded that raising the heat source temperature has a larger influence in the lower temperature range investigated [39]. In another study conducted by Wang et al., a Pilot-Scale Hydrate Simulator (PHS), a three-dimensional 117.8 L pressure vessel, was applied in order to study the methane hydrate dissociation below the quadruple point in a sandy sediment. The lower pressure enhanced the rate of ice formation, which caused larger hydrate dissociation rate. When the pressure is lower than the quadruple point, ice will more easily form at a lower initial reservoir temperature, which leads to a higher hydrate dissociation rate [40]. When the pressure is lower than the quadruple point, ice will be easy to form in a lower initial reservoir temperature, which leads to a higher hydrate dissociation rate. Song et al. characterized the gas production processes from methane hydrate in porous media using depressurization, two-cycle warm-water injection and a combination of the two methods. The experimental results for the depressurization method proved that the depressurization method was efficient in the earlier stage of gas production. However, the rate of gas production decreased as the temperature decreased [41].

5. Gas production

Gas production potential of Mt. Elbert hydrate deposit and other North Slope accumulations has been evaluated by solving mass and heat balance coupled equations and modeling non-isothermal gas release, phase behavior and heat under conditions of common natural methane (CH_4)-hydrate-bearing deposits in complex formations [42–46]. Santamarina et al. simulated gas production during depressurization, heating, and CO_2-CH_4 replacement using the 2-D experiments data. In this study, simulation of thermodynamics and the transport process of hydrate dissociation has been used [45]. Comparative study of the conventional and innovative approaches for producing methane gas from gas hydrate-bearing geologic reservoirs, using numerical simulation, has been accomplished by Bahangale et al. [46] and Phale et al. [47]. One comparative study of several depressurization and thermal injection numerical models has been conducted by Sawyer [48]. Moridis et al. developed a module to model the non-isothermal methane gas release [44]. The goal of this study is to analyze various gas production scenarios from five methane hydrate-bearing zones at the Mallik site in Canada. Discoveries in zone #1, have shown that gas production from hydrate sediments is possible through depressurization and making a thin gas-free zone at the base of the hydrate stability field. Studies in zone #2 show that the gas hydrate layer, could produce significant amounts of gas. In zones #3, #4 and #5, circulation of hot water in well has been used to initiate the dissociation process. Khataniar et al. conducted an analytical approach to model the gas hydrate production during hydrate decomposition [49].

6. Utilization of SOFC systems

SOFC systems have been operated as steady-state base-loaded generators and usually not at very high pressures like that exists in deep ocean environments [50–52]. SOFC and PEM in electrolysis mode have been shown in lab-scale applications and no measurement of their long term or high pressure characteristics is reported [53,54]. Limited experimental and theoretical investigations of high pressure operation of SOFC/SOEC have been studied [55–58]. Operation of other types of fuel cells, such as alkaline and PEM electrolyzers under high pressure operating conditions has been reported in [52,54,59–61].

A strategy that we propose in this study for the methane hydrate dissociation, is the in-situ utilization of integrated electrochemical systems based primarily upon the use of high temperature solid oxide fuel cell (SOFC) technology. These systems have unique features of efficient electricity production from a portion of the released gases, and heat provision for methane hydrate gas dissociation.

Solid oxide fuel cell (SOFC) technology is an electrical power generation technology. SOFC directly converts fuel to electricity. The direct electrochemical reaction of fuel and oxygen results in

high fuel-to-electric conversion efficiencies with no pollutant emissions such as carbon dioxide. FuelCell Energy, VersaPower, Bloom Energy, and Solid Power are among many companies that have been developing and commercializing SOFC technology during recent years. The power range that many companies have demonstrated is in the range of (1–5 kW), and distributed generation scale (100–800 kW) in SOFC systems that have shown high efficiency and low pollutant emissions [62–64]. Some companies have demonstrated 200–330 kW pressurized SOFC/gas turbine hybrid systems (e.g., LG Fuel Cell and Siemens Power). The most common anode materials for fuel oxidation in SOFC systems are nickel/yttria-stabilized zirconia (Ni/YSZ) cermets that have excellent catalytic activity. Ni/YSZ anode has some disadvantages, such as carbon deposition, sulfur poisoning and nickel coarsening that make direct using of natural gas not feasible. Perovskite oxides like donor-doped $SrTiO_3$ are alternative SOFC electrode materials [65–69].

The novelty of this work is using thermodynamic and heat transfer principles to analyze an integrated SOFC methane hydrate bed system at high pressure of *100 bar* at which methane hydrates are possibly stable in the phase diagram. Understanding the operational feasibility of high pressure SOFC systems and their dynamics could allow their integration and use in the systems of methane gas extraction from deep ocean hydrate sediments. While we do not currently propose to experimentally determine the performance characteristics of these systems, we believe that it is important to determine the feasibility of such systems to see if it would be worth to develop such capabilities for future methane recovery systems.

7. Model description

7.1. Power generation

One of the main objectives of this study is to evaluate the potential electric power production for deep ocean electronic and screening devices, particularly those with greater electrical power requirements than batteries can typically supply. The current effort envisions, simulates, and analyzes an integrated SOFC system that produces a maximum power of 1000 W as integrated with a deep ocean methane hydrate bed. The focus of this study is to propose a sustainable power generating system based on SOFC that requires low maintenance and operates on the recovered methane gas to be used in the steam methane reformer. The immediate use of methane gas in the reformer eliminates the long distance electrical cabling complications associated with the use of batteries instead of fuel cell systems in applications such as underwater sensors. This overall in-situ system design is unique to fuel cell systems.

7.2. Fuel production

Another objective of this effort is to determine if a sufficient amount of fuel for system operation and additional production of methane gas for other uses is possible with the SOFC system envisioned. In this case, only a portion of the extracted methane gas would be delivered to the SOFC system for power and electricity generation for end-use. The primary functions that need to be performed by the electrical power generation system are gas purification and steam methane reforming (SMR) to produce hydrogen at a

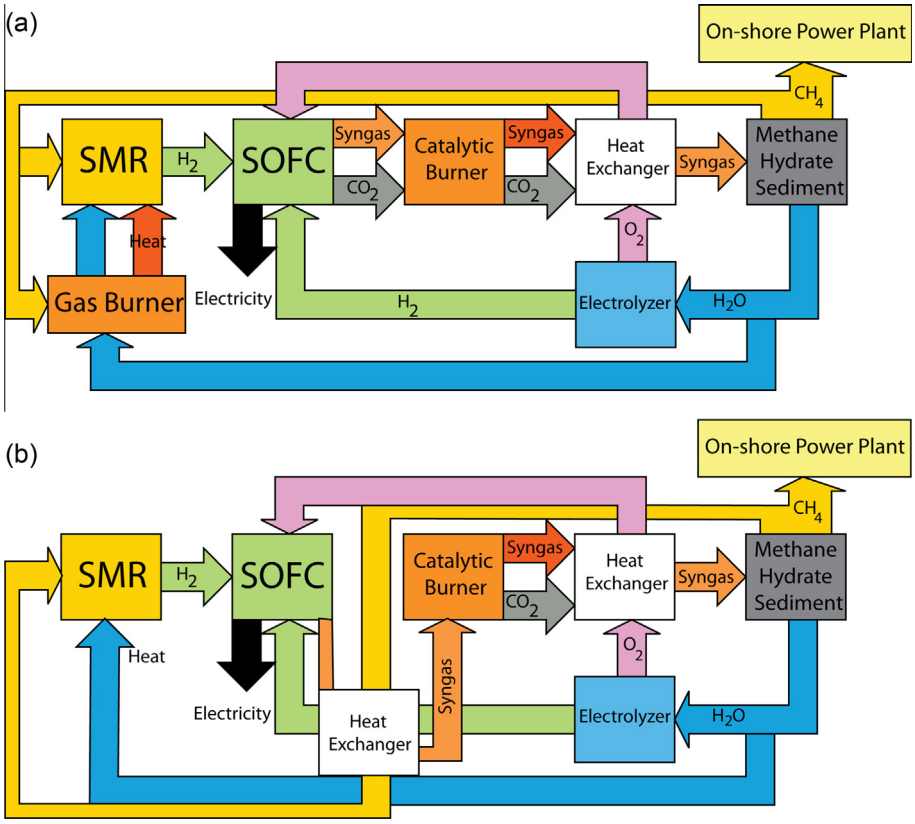

Fig. 1. These concepts are related to oxygen production by water electrolysis. In this case, water is produced from dissociated sediments: (a) Integrated SOFC system: SMR heat is provided by burning part of the dissociated methane in the gas burner (Case 1): in this method, all the heat required by the SMR unit is provided by burning the methane gas in the gas burner. The heat exchange process occurs through a heat exchanger not shown in the figure. Gas burner will be used as a heat exchanger to preheat the water before entering the SMR unit. (b) Integrated SOFC system: SMR heat is provided by heat exchange from effluent gases of SOFC (Case 2): As shown in the figure the heat exchanger preheats the extracted methane from methane sediments before entering the SMR unit.

sufficient flow rate for electricity generation through an electrochemical reaction in the fuel cell. A catalytic steam reformer is simulated to provide a hydrogen-rich gas for the solid oxide fuel cell at a sufficient flow rate to sustain the system maximum net power production of 1000 W. The methane gas required for the steam reformer operation is provided by a portion of the extracted methane gas from hydrate layer. Oxidant supply and heat exchangers are other ancillary parts of the system that are simulated. The SOFC system has been chosen in this study due in part to their ability to tolerate both CO and methane in the anode compartment and because they operate at high temperatures for improved electrochemical kinetics. The fuel supply system is assumed to possess equipment to collect and clean the dissociated methane gas. Finally, the SOFC is used as a thermal heat source to provide an adequate amount of heat for hydrate layer dissociation and methane gas production in the integrated system model.

7.3. Cycle conceptualization

Figs. 1–3 show a system cycles in which, a portion of the extracted methane gas from the hydrate sediment is used to provide the required methane gas for the steam methane reformer at a sufficient mass flow rate. Since the SMR catalytic reaction is endothermic, two main system cases have been studied regarding the energy provision for the SMR reactor.

Case 1: Fig. 1a shows the system schematic in which a portion of the dissociated methane gas is used to provide heat for the steam methane reformer through combustion in a gas burner. *Case 2:* Fig. 1b shows the system case in which the heat for the steam methane reformer is provided through heat exchange with the heat in the effluent gases of SOFC. Note that in this case there will be less heat available for methane dissociation.

This study involves a combination of possible dissociation mechanisms including depressurization and thermal stimulation.

Three main system configurations for oxygen delivery are conceptualized. The first concept is associated with oxygen production by electrolyzing the recovered water from the dissociated methane gas. The second concept is associated with the oxygen delivery from the on-shore power plant following by an oxygen liquefaction unit. The third concept is associated with the oxygen production by saline sea water electrolysis through alkaline electrolysis process. It is important to mention that the energy requirement for the oxygen liquefaction process has not been calculated in the net process as the process takes place at the on-shore power plant.

The assumption that has been made in this study is that all of the methane gas that could be recovered by thermal stimulation and depressurization from methane hydrate sediments, can be used in steam methane reformer (SMR unit). It is assumed that using correct insulation and piping system, all the methane gas can be recovered. Therefore, this study could be a good measure of maximum power generated by SOFC for future studies that will use solid oxide fuel cell and balance of plant (BOP) as the main process of hydrate recovery.

One major contribution of this study is to determine the potential natural gas production over a specified period of time (i.e., 120 days), as the previous experimental studies show that 120 continuous days of gas recovery was possible.

7.4. Non-isothermal system formulation

The energy equation is obtained by applying the law of conservation of energy to a small element of volume in the methane hydrate bed. Both kinetic and internal energy enter and leave the system by convective transport. The rate of increase of kinetic

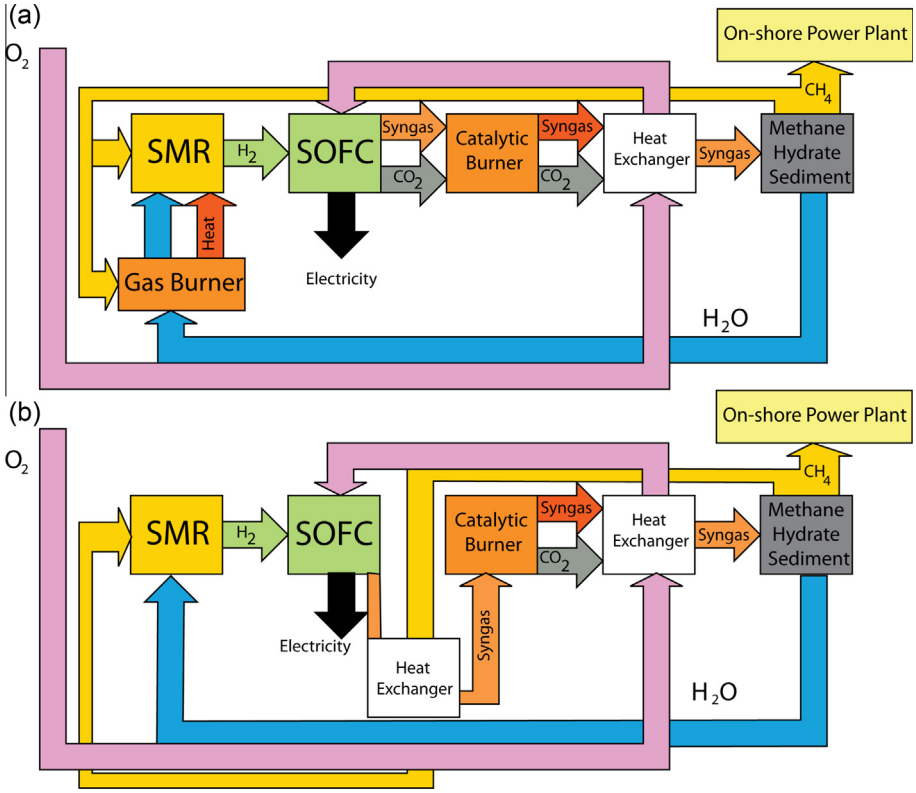

Fig. 2. In this case, oxygen is delivered from the on-shore power plant following by oxygen liquefaction process. The remaining system concepts are same as what are shown in Fig. 1. (a) Integrated fuel cell system: SMR heat provided by burning part of the dissociated methane in the gas burner (Case 1). (b) Integrated fuel cell system: SMR heat provided by heat exchange from effluent gases of the SOFC (Case 2).

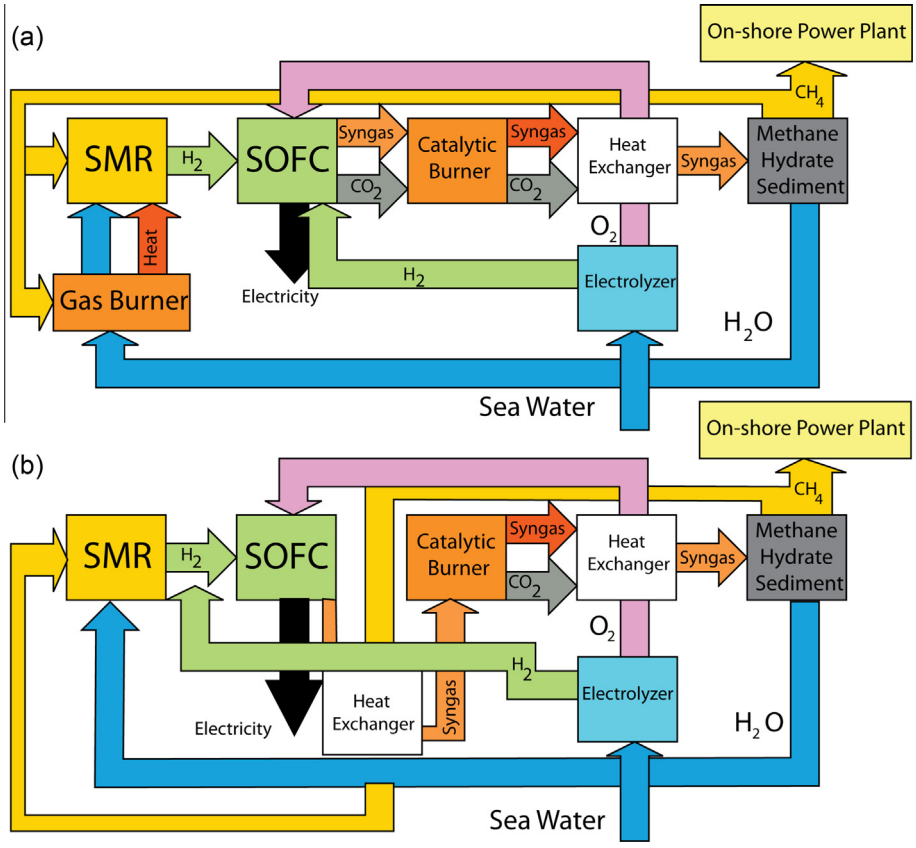

Fig. 3. The figure shows electrolysis using saline sea water in order to produce oxygen for the SOFC operation. The remaining system concepts are the same as those shown in Figs. 1 and 2. (a) Integrated fuel cell system: SMR heat provided by burning part of the dissociated methane in the gas burner (Case 1). (b) Integrated fuel cell system: SMR heat provided by heat exchange from effluent gases of SOFC (Case 2).

and internal energy within the volume element is in the form of Eq. (1) [70]:

$$\Delta x\Delta y\Delta z\frac{\partial}{\partial t}\left(\frac{1}{2}\rho v^2+\rho\hat{u}\right) \tag{1}$$

where $\hat{u}$ is the internal energy per unit mass (i.e., specific internal energy). Thus, $\rho\hat{u}$, is the internal energy per unit volume. $\frac{1}{2}\rho v^2$ represents the kinetic energy per unit volume.

Eq. (2) describes the energy equation in the enthalpy form:

$$\rho\frac{DH}{Dt}=-(\nabla\cdot\vec{q})-(\tau:\nabla\vec{v})-\left(\frac{\partial\ln P}{\partial\ln T}\right)_p\frac{DP}{Dt} \tag{2}$$

Eq. (2) is the equation of change for temperature, in terms of heat flux vector q and the viscous momentum flux, τ.

7.5. One-dimensional hydrate bed model

Fig. 4 shows the model for the hydrate dissociation process that is simulated after the method of Selim and Sloan [22], in which gas and water are produced at the moving boundary (i.e., dissociation front). The porous medium is initially at a uniform temperature T_i, which occupies the semi-infinite region, $0<x<\infty$. At time $t=0$, the temperature at the boundary $x=0$ rises to the SOFC system exit temperature. It is worth noting that the hydrate formation and SOFC system exit gases are in thermal equilibrium during the system operation. The temperature at $x=0$ is constant during the dissociation process, since the fuel cell system operates steadily. The temperature of the fuel cell system exit gases are at a higher temperature than the hydrate dissociation temperature (T_D) and the hydrate initial temperature (T_i), thus, the moving boundary (i.e., dissociation front) starts moving at the time $t=0$. Therefore, at any time t the hydrate formation is separated into two distinct zones. Zone 1: contains the dissociated water and methane gas. Zone 2: contains the non-dissociated hydrate formation. Thus, in mathematical terms, at any specific time t, in the 1-D physical model, zone 1 fills the region $0<x<X(t)$ and the zone 2 fills the region $X(t)<x<\infty$, where, $X(t)$ expresses the moving boundary position. The major assumptions associated with this model are:

(1) the water that is dissociated from the hydrate formation is stationary,
(2) thermophysical properties of each phase are uniform and in equilibrium,
(3) viscous dissipation and inertial forces are negligible,

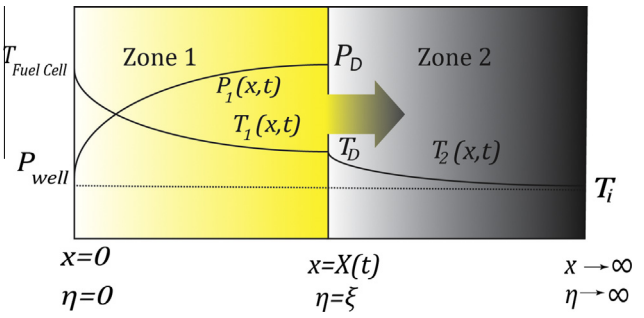

Fig. 4. One dimensional model of hydrate dissociation due to temperature increase or pressure drop proposed by Selim and Sloan [22].

(4) external energy transmission is neglected,
(5) the dissociation front is in equilibrium and dissociation occurs immediately, and
(6) gas phase is in thermal equilibrium with the sediment temperature.

The purpose of this work is to integrate the semi-analytical model developed by Selim et al. for hydrate dissociation under chemical equilibrium with an SOFC model that is used to stimulate hydrate dissociation by the SOFC generated heat.

7.6. Thermal stimulation mathematical model formulation

In this section, relevant parts of the one dimensional model of hydrate dissociation under thermal stimulation in porous media, developed by Selim and Sloan [22] are summarized (see Appendix A for more details). The continuity equation throughout the dissociated zone (water and gas zone) is in the form of Eq. (3).

$$\varepsilon\frac{\partial\rho_g}{\partial t}+\frac{\partial(\rho_g v_x)}{\partial x}=0,\quad 0<x<X(t) \tag{3}$$

where ε expresses the porosity of the hydrate reservoir, ρ_g is the methane gas density and v_x is the gas axial velocity in zone 1. The momentum equation in the gas phase and Darcy's law for the dissociated gas in zone 1 are in the form of Eq. (4):

$$v_x=-\frac{\zeta}{\mu}\frac{\partial P}{\partial x},\quad 0<x<X(t),\quad t>0 \tag{4}$$

where P describes the pressure distribution in zone 1. μ is the methane gas viscosity and ζ is the sediment permeability. The energy balance in zone 1 is in the form of Eq. (5):

$$\rho_I C_{p,I}\frac{\partial T_I}{\partial t}+\frac{\partial(\rho_g C_{p_g} v_x T_I)}{\partial x}=k_I\frac{\partial^2 T_I}{\partial x^2}\quad 0<x<X(t),\quad t>0 \tag{5}$$

where T_I represents the temperature profile in zone 1. k_I is thermal conductivity of zone 1. $C_{p,g}$ is the methane gas heat capacity. The energy balance in the non-dissociated zone (i.e., zone 2) is in the form of Eq. (6):

$$\frac{\partial T_{II}}{\partial t}=\alpha_{II}\frac{\partial^2 T_{II}}{\partial x^2}\quad X(t)<x,\quad t>0 \tag{6}$$

where T_{II} represents the temperature profile in the non-dissociated zone, and α_{II} is the thermal diffusivity of zone 2. Boundary conditions for the initial value problem are in the form of Eqs. (7)–(9):

$$T=T_{FC}\quad x=0,\quad t>0 \tag{7}$$

$$P=P_w\quad x=0,\quad t>0 \tag{8}$$

where T_{HX} is the system heat exchanger exit temperature, and P_w represents the production well pressure. Because continuity, temperatures of the two zones are identical on the dissociation front, thus:

$$T_I=T_{II}=T_D\quad x=X(t),\quad t>0 \tag{9}$$

The mass balance at the moving boundary position is in the form of Eq. (10):

$$\Omega\varepsilon\rho_{Hydrate}\frac{dX}{dt}+\rho_g v_x=0\quad x=X(t),\quad t>0 \tag{10}$$

where Ω is the mass of methane gas per unit mass of the hydrate formation and the number is found in the literature to be 0.1265 kg methane per kg hydrate [22]. The energy balance at the dissociation front is in the form of Eq. (11):

$$k_I\frac{\partial T_I}{\partial x}-k_{II}\frac{\partial T_{II}}{\partial x}=-\varepsilon\rho_{Hydrate}\Delta H_D\frac{\partial X}{\partial t}\quad x=X(t),\quad t>0 \tag{11}$$

where k_1 and k_2 are the thermal conductivities of zone 1 and zone 2, and ΔH_D is the methane hydrate heat of dissociation, which has a temperature dependence. The thermodynamic equilibrium relation between the hydrate dissociation temperature, T_D, and pressure P_D at the dissociation interface is expressed as Eq. (12):

$$P_D=\exp\left(A_D-\frac{B_D}{T_D}\right)\quad x=X(t),\quad t>0 \tag{12}$$

Boundary conditions for the non-dissociated zone are shown in Eqs. (13)–(15):

$$T_{II}=T_i\quad x\to\infty\quad t>0 \tag{13}$$

$$T_{II}=T_i\quad 0<x<\infty,\quad t=0 \tag{14}$$

$$X(t)=0\quad t=0 \tag{15}$$

where the Π parameter (i.e., non-dimensioned distance) can be determined from Eq. (16):

$$x=\Pi\sqrt{4\alpha_{II}t} \tag{16}$$

Table 1
Methane hydrate properties used in the one dimensional thermal stimulation modeling [22].

Parameter	Value
Porosity, ε	0.3
Permeability, κ	1.38×10^{-13} m^2
Thermal diffusivity of the dissociated zone, α_I	$2.89\times10^{-6}\ \frac{m^2}{s}$
Thermal diffusivity of hydrate zone, α_I	$6.97\times10^{-7}\ \frac{m^2}{s}$
Thermal conductivity of the dissociated zone, k_1	$5.57\ \frac{W}{m\,K}$
Thermal conductivity of the undissociated zone, k_2	$2.73\ \frac{W}{m\,K}$
Hydrate density, ρ_H	$913\ \frac{kg}{m^3}$
$\Delta H_D\left(\frac{J}{kg}\right)$ for $248<T<273$ K	$215.59\times10^3-394.945T$
$\Delta H_D\left(\frac{J}{kg}\right)$ for $273<T<298$ K	$446.12\times10^3-3132.638T$
Thermal equilibrium equation of hydrate (Phase diagram)	$P_D=\exp\left(49.3185-\frac{9459}{T_D}\right)Pa$
Gas heat capacity $\left(\frac{J}{kg\,K}\right)$	$C_{pg}=1.23879\times10^3+3.1303T+7.905\times10^{-4}T^2-6.858\times10^{-7}T^3$
Gas viscosity (Pa s)	$\mu=[2.4504\times10^{-3}+2.8764\times10^{-5}T+3.279\times10^{-9}T^2-3.7838\times10^{-12}T^3]+\left[2.0891\times10^{-5}\rho_g+2.5127\times10^{-7}\rho_g^2-5.822\times10^{-10}\rho_g^3+1.8387\times10^{-13}\rho_g^4\right]$

Table 2
Solid oxide fuel cell properties used in the modeling for two cases of (a) and (b).

Parameter	Value used
Temperature	700 °C
Anode exchange current density ($j_{0,anode}$)	10 $\frac{A}{cm^2}$
Cathode exchange current density ($j_{0,cathode}$)	0.1 $\frac{A}{cm^2}$
α_{O_2}	0.5
α_{H_2}	0.5
ASR_{ohmic}	0.04
Limiting current density (j_L)	2 $\frac{A}{cm^2}$
$S(H_2O)$	193.71 $\frac{J}{mol\ K}$
$S(H_2)$	128.25 $\frac{J}{mol\ K}$
$S(O_2)$	205.18 $\frac{J}{mol\ K}$
Y_1	$-\frac{RT\ln(j_{0,anode})}{\alpha nF}$
Y_2	$\frac{RT}{\alpha_{H_2} nF}$
Y_3	$-\frac{RT\ln(j_{0,cathode})}{\alpha nF}$
Y_4	$\frac{RT}{\alpha_{O_2} nF}$
Y_5	$\frac{RT}{nF}\left(1+\frac{1}{\alpha}\right)$

Hence, the dissociation front position is in the form of Eq. (17):

$$X(t) = \Xi\sqrt{4\alpha_{II}t} \tag{17}$$

and Ξ is determined by solving the system of equations presented in Appendix A.

It should be noted that, the temperature of dissociation T_D and the pressure of dissociation P_D are independent of time. Thus, we can conclude that they are constant during the dissociation process. The properties of the methane hydrate reservoir that are used in the simulations are shown in Table 1.

7.7. Depressurization modeling

In this section, parts of the mathematical formulation and classical Stefan's problem for hydrate decomposition suggested by Makogon [71] that are used in the current simulations are summarized. Additional details are presented in Appendix B.

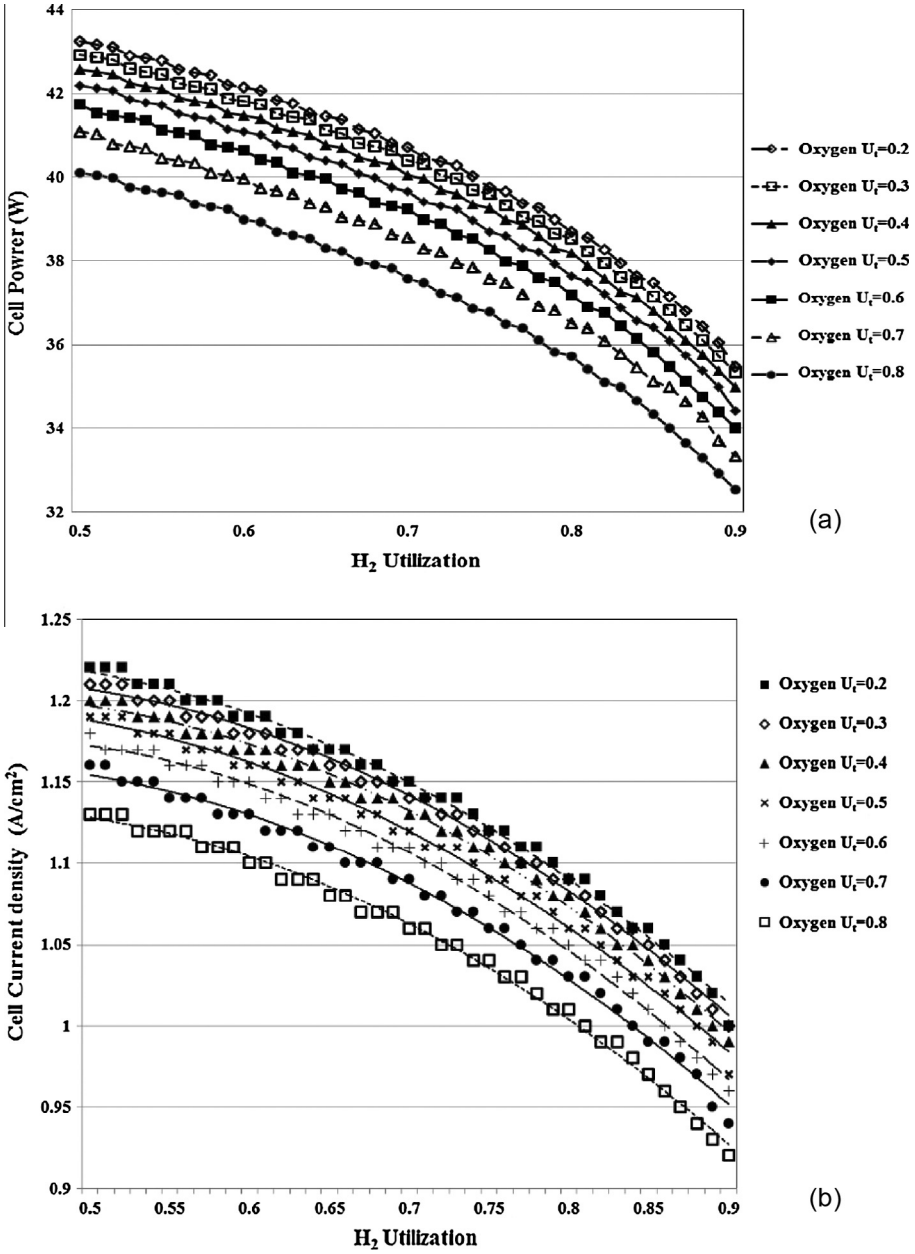

Fig. 5. (a) SOFC power at different levels of hydrogen and oxygen utilizations. (b) SOFC current density at different levels of hydrogen and oxygen utilizations.

The boundary conditions for depressurization modeling are described in Eqs. (18)–(22):

$$P_1(0,t) = P_w \tag{18}$$

$$P_2(x,0) = P(\infty,t) = P_i \tag{19}$$

$$P_1(X(t),t) = P_2(X(t),t) = P_D(T_D) \tag{20}$$

$$T_2(\infty,t) = T(x,0) = T_i \tag{21}$$

$$T_1(X(t),t) = T_2(X(t),t) \tag{22}$$

where P_i and T_i are the initial pressure and temperature of the hydrate layer at $t = 0$. $P_D(T_D)$ represents the equilibrium relation between the pressure and temperature of hydrate decomposition T_D at the dissociation front (see Appendix B). This relation is derived from the thermodynamic equilibrium between methane vapor and methane hydrate.

At the dissociation front $X(t)$, the conditions of gas and water mass balance should be considered. The term mass fraction of gas in the hydrate is introduced by Bondarev et al. [72] as follows expressed in Eq. (23):

$$\theta = \frac{M_{gas}}{N_m \cdot M_{water} + M_{gas}} \tag{23}$$

M_{gas} and M_{water} are the molecular weight of methane and water, respectively. N_m is the number of water molecules per one molecule of gas in the hydrate structure (i.e., hydration number). The mass balance for the gas at the dissociation front location $X(t)$ is derived as Eq. (24) [73]:

$$\rho_1 v_1 - \rho_2 v_2 = -[\beta\theta\rho_3 - (1-\tau)\rho_1 + (1-\beta)\rho_2]\varepsilon\frac{dX(t)}{dt} \tag{24}$$

where ρ_1 and ρ_2 are the densities of the methane gas in the dissociated and non-dissociated zones, and v_1 and v_2 are the velocities of the methane gas in the dissociated and non-dissociated zones, respectively. Using the equation of state for gas and the continuity equation at (t), Eq. (25) is obtained:

$$\rho_1(X(t),t) = \rho_2(X(t),t) = \rho_0\frac{P_D T_0}{Z P_0 T_D} \tag{25}$$

where Z is the compressibility factor of gas, and ρ_0 is the density of gas at atmospheric pressure P_0 and temperature T_0. Hence, the equation for gas balance at the decomposition front is in the form of Eq. (26):

$$v_1(X(t),t) - v_2(X(t),t) = -\left[\theta\beta\frac{\rho_3 P_0 T_D}{\rho_0 P_D T_0}z - (\beta-\tau)\right]\varepsilon\frac{dX(t)}{dt} \tag{26}$$

Eq. (27) describes the mass balance of water released from the hydrate sediment during the dissociation process.

$$\rho_W\varepsilon\tau = (1-\theta)\rho_3\varepsilon\beta \tag{27}$$

It has been assumed that the water is stationary, and the pressure and temperature are low enough in the gas hydrate layer. Thus, we can assume ρ_W and τ_W are also constant. The temperature field of the gas-saturated layer can then be expressed by Eq. (28):

$$a_n\frac{\partial^2 T_n}{\partial x^2} = \frac{\partial T_n}{\partial t} - \frac{c_v k_n}{c_n\mu}\frac{\partial P_n}{\partial x}\left(\frac{\partial T_n}{\partial x} - \delta\frac{\partial P_n}{\partial x}\right) - \eta\frac{\varepsilon_n c_v}{c_n}\frac{\partial P_n}{\partial t} \tag{28}$$

where a_n and c_n are the thermal conductivity and the heat capacity, respectively, of the zones 1 and 2. c_v is the volumetric heat capacity of methane gas, and δ, and η are the throttling and adiabatic coefficients of the gas, respectively. The dissociation front position can then be expressed by Eq. (29):

$$X(t) = \sqrt{\sigma t} \tag{29}$$

where σ is determined by solving the systems of equation (see Appendix B).

Assuming that conductive heat transfer is much smaller than convective heat transfer, Eq. (28) can be written in the form of Eq. (30):

$$\frac{\partial T_n}{\partial t} - \frac{c_v k_n}{c_n\mu}\frac{\partial P_n}{\partial x}\left(\frac{\partial T_n}{\partial x} - \delta\frac{\partial P_n}{\partial x}\right) - \eta\frac{\varepsilon_n c_v}{c_n}\frac{\partial P_n}{\partial t} = 0 \tag{30}$$

P_D, T_D and σ, which govern the rate of dissociation front movement, are determined from Eq. (31):

$$T_D = T_i - A_2\delta\left[erfc\quad \kappa_2 - \Phi_2(\kappa_2) - \frac{\eta}{\delta}B_2\Phi_2(\kappa_2)\right] \tag{31}$$

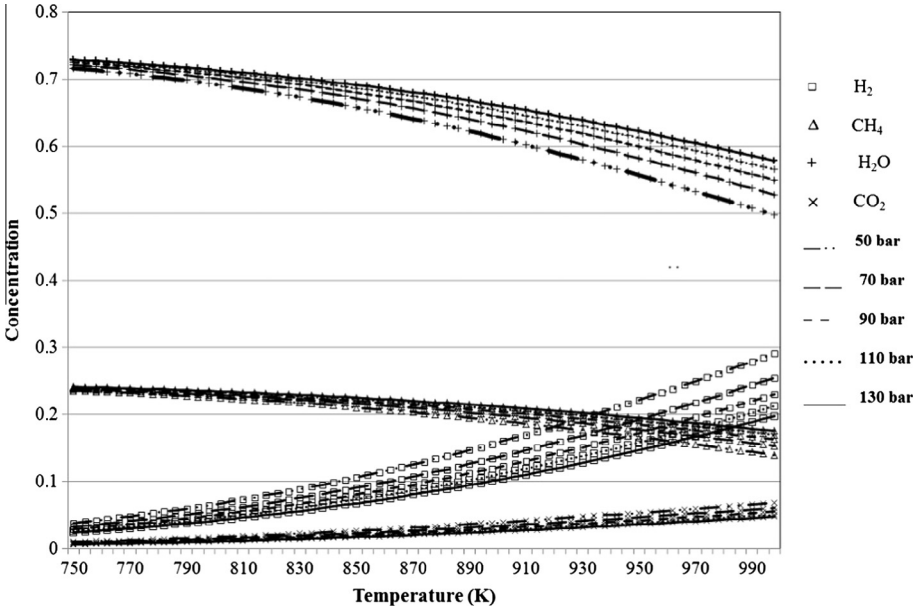

Fig. 6. Variation of SMR equilibrium concentration in temperature range of [750–1000] K.

The pressure at the dissociation front is found from Eq. (26).

It should be noted that the temperature and the pressure at the dissociation front are fixed values and they depend upon the magnitude of well pressure, P_w. The production rate of gas per unit length of well can then be derived in the form of Eq. (32):

$$Q = -\frac{k_1}{\mu}\frac{\partial P(0,t)}{\partial x} = \frac{k_1}{\mu}\frac{\left(P_D^2 - P_w^2\right)}{P_w}\frac{1}{erf\kappa_1}\frac{1}{2\sqrt{\pi\Lambda_1 t}} \tag{32}$$

The production rate of gas decreases inversely with time. These equations can be used to determine all the characteristics of the process of gas hydrates dissociation during depressurization.

7.8. Fuel cell system modeling

Operating the solid oxide fuel cell at high pressure has a beneficial effect on the fuel cell electrochemical conversion efficiency, which depends upon the partial pressures of the reactants (and

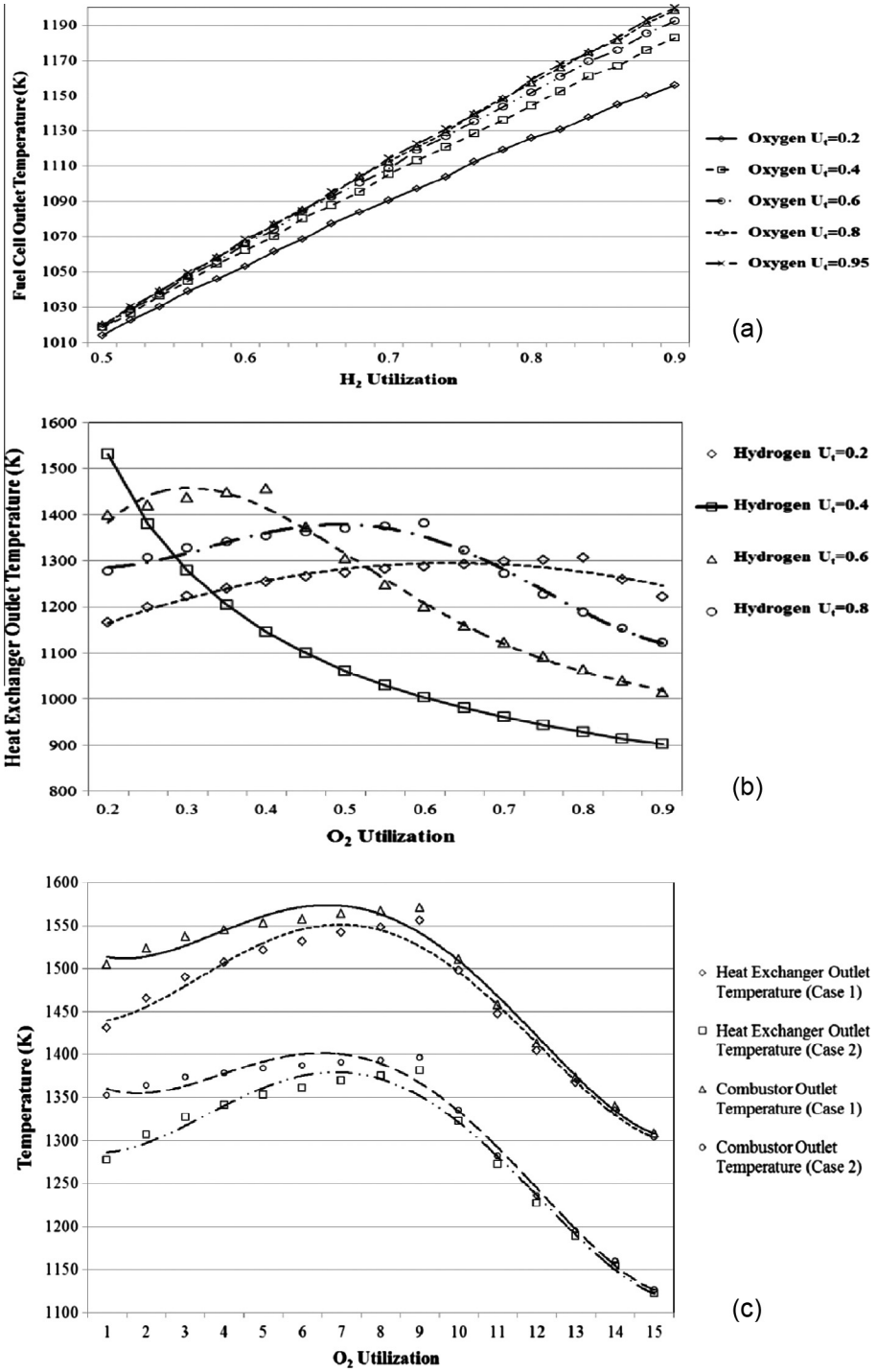

Fig. 7. (a) SOFC exit temperature change as a function of hydrogen utilization, (b) heat exchanger outlet temperature change as a function of oxygen and hydrogen utilization and (c) combustor and heat exchanger exit temperature change as a function of hydrogen and oxygen utilization for case 1 and case 2 at hydrogen utilization of 0.6.

products). Since the behavior of the reactants and products at the very high pressures of the deep ocean environment are different from the ideal behavior, the fugacity coefficients should be computed. The compressibility of real gases is estimated based on second virial coefficients of the Van der Waals equation of state from Eq. (33):

$$Z = \frac{P\overline{V}}{RT} = \left(1 + \frac{B_{2V}(T)}{\overline{V}} + \frac{B_{3V}(T)}{\overline{V}^2} + \cdots\right) = 1 + \left(b - \frac{a}{RT}\right)\frac{1}{\overline{V}} + \frac{b^2}{\overline{V}^2} + \cdots \quad (33)$$

where Z is the compressibility factor of the real gas, and a and b are parameters of the Van der Waals equation of state. The fugacity coefficient relation with real partial pressures of the gases is then represented in the form of Eq. (34):

$$\ln\gamma = \ln\frac{f}{P} = \int_0^P \frac{Z-1}{P'}dP' \quad (34)$$

Alternatively, Eq. (35) can be used:

$$\gamma = \frac{f}{P} = \exp\left[\left(b - \frac{a}{RT}\right)\frac{P}{RT}\right] \quad (35)$$

The entropy of reactant and product gases of the fuel cell at the specified pressure of 100 bar are calculated from of Eq. (36):

$$s - s^\circ = \bar{s}_2^\circ - \bar{s}_1^\circ - R_u \ln\frac{P_2}{P_1} \quad (36)$$

where s° is the entropy at standard temperature and pressure, and $\bar{s}^\circ$ is the entropy that is independent of pressure. Pressurizing the fuel cell system in order to increase the reactant partial pressures, will potentially increase the reversible voltage. However, due to the logarithmic nature of the voltage dependence upon pressure, improvement will be slight. A total electrochemical reaction that is considered in SOFC is the reaction between fuel (i.e., hydrogen in the reformate) and oxygen in the form of Eq. (37):

$$H_2 + \frac{1}{2}O_2 \rightarrow H_2O \quad (37)$$

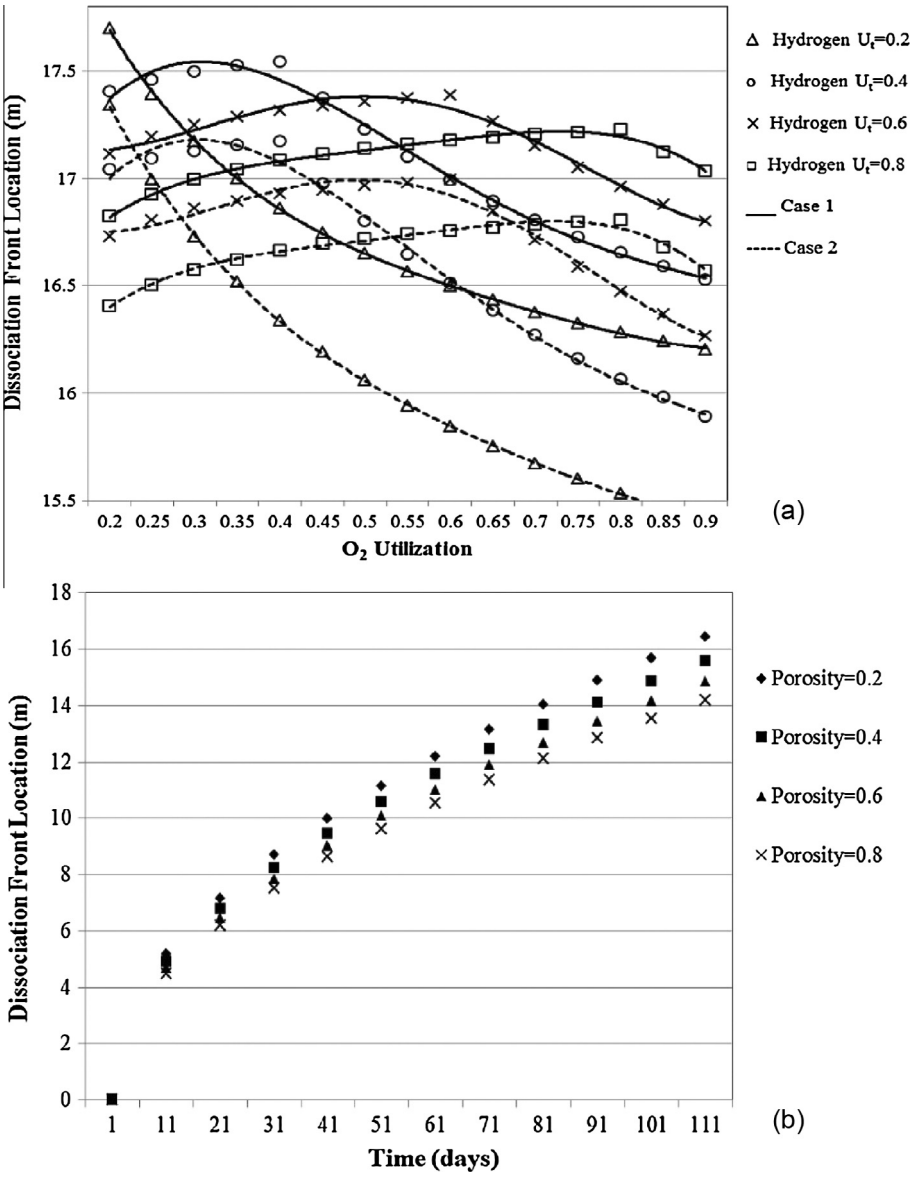

Fig. 8. (a) Dissociation front location as a function of hydrogen and oxygen utilization. (b) Dissociation front location in hydrate layer during time at different porosities (Hydrogen utilization = 0.6, Oxygen Utilization = 0.5).

The Nernst potential, Eq. (38), which expresses the maximum thermodynamic voltage, has been calculated as a function of the entropy difference between reactants and products of the electrochemical reaction, fugacity of the reactants and products and the operating temperature of SOFC, which is considered to be 700 °C.

$$E_{Nernst} = E^{\circ} + \frac{\Delta s}{nF}(T - T_0) - \frac{RT}{nF}\ln\frac{f_{H_2O}}{f_{H_2} f_{O_2}} \tag{38}$$

where n is the number of electrons transferred in the electrochemical reaction, F is the Faraday constant, and f_{H_2O}, f_{H_2} and f_{O_2} are the fugacities of the gases involved in the cell electrochemical reactions. The activation polarization of the SOFC is modeled using the Butler-Volmer equation that is described in Eq. (39):

$$j = j_0\left(e^{\frac{\alpha nF\eta}{RT}} - e^{\frac{-(1-\alpha)nF\eta}{RT}}\right) \tag{39}$$

In Eq. (39), j_0 represents the exchange current density of the fuel cell, α is the electron transfer coefficient, and η expresses the activation polarization of the cell. The Ohmic polarization of the fuel cell is simulated in the form of Eq. (40):

$$\eta_{ohmic} = i(R_{electrode} + R_{ionic}) \tag{40}$$

where $R_{electrode}$ and R_{ionic} are the combined electronic and iconic resistances of electrode and interconnects and the ionic resistance of the electrolyte, respectively. Typically, the electrode and interconnect resistances are negligible compared to the ionic resistance. Thus, it is assumed that one overall cell resistance that has the temperature dependence of ionic resistance in the electrolyte characterizes all of the Ohmic losses simulated in this study. Eq. (41) describes the mass concentration polarization:

$$\eta_{conc} = \frac{RT}{nF}\ln\frac{j_L}{j_L - j} \tag{41}$$

j_L and j are the limiting current density and the current density of the fuel cell. Hence, total voltage of the cell is described in terms of the different types of polarizations and losses of the fuel cell and the thermodynamic voltage (i.e., Nernst potential) as shown in Eqs. (42) and (43):

$$V = E_{thermo} - \eta_{act,anode} - \eta_{act,cathode} - \eta_{ohm} - \eta_{conc} \tag{42}$$

Or:

$$V = E_{thermo} - (Y_1 + Y_2\ln j) - (Y_3 + Y_4\ln j) - jASR_{ohmic} - Y_5\ln\frac{j_L}{j_L - j} \tag{43}$$

where Y_1, Y_2 represent the activation polarization constants of the anode compartment. Similarly, Y_3, Y_4, represent the activation polarization constants of the cathode compartment, which could be determined from the Butler-Volmer equation. Y_5 is the mass concentration polarization constant. The values of these constants that are used in the present study are presented in Table 2.

Enthalpies of the real gases involved in the reactions are developed based upon pressure, temperature and the second virial coefficients of the Van der Waals equation of state, at high pressure for the steam methane reformer in Eqs. (44) and (45).

$$\left(\frac{\partial h}{\partial P}\right)_T = v - T\left(\frac{\partial v}{\partial T}\right)_P \tag{44}$$

$$H = H^{\circ} + B(T)P - T\frac{\partial B(T)}{\partial T} \tag{45}$$

Eqs. (46) and (47) determine the partial pressures of the hydrogen entering the SOFC anode compartment, and the water in fuel cell exit, assuming the ideal gas law:

$$P_{H_2} = P \times \frac{(1 - U_{f,H_2}) \times \dot{N}_{H_2,SMR}}{\dot{N}_{H_2O_{SMR}} + (1 - U_{f,H_2}) \times \dot{N}_{H_2,SMR} + \dot{N}_{CO_2,SMR} + \dot{N}_{CO_{SMR}} + \dot{N}_{CH_4,SMR} + \dot{N}_{H_2O_{prod}}} \tag{46}$$

$$P_{H_2O} = P \times \frac{\dot{N}_{H_2O_{SMR}} + \dot{N}_{H_2O_{prod}}}{\dot{N}_{H_2O_{SMR}} + (1 - U_{f,H_2}) \times \dot{N}_{H_2,SMR} + \dot{N}_{CO_2,SMR} + \dot{N}_{CO_{SMR}} + \dot{N}_{CH_4,SMR} + \dot{N}_{H_2O_{prod}}} \tag{47}$$

where P is the total operating pressure of the SOFC and the steam reformer. $\dot{N}_{H_2,SMR}$, $\dot{N}_{CO_2,SMR}$, $\dot{N}_{CO_{SMR}}$, $\dot{N}_{CH_4,SMR}$, $\dot{N}_{H_2O_{SMR}}$ describe the molar flows of hydrogen, carbon dioxide, carbon monoxide,

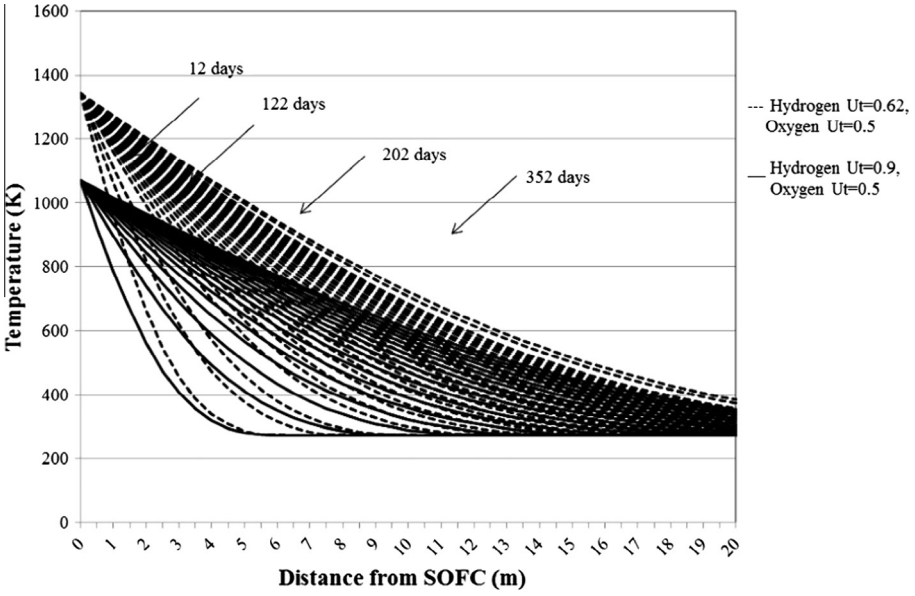

Fig. 9. Temperature development in the hydrate layer varying with distance from the fuel cell system for H_2 utilization = 0.62, O_2 utilization = 0.5 and H_2 utilization = 0.9, O_2 utilization = 0.5.

methane and water in the steam reformer exit that enters the anode component of the fuel cell. $\dot{N}_{H_2O_{SMR}}$ is the water produced in the anode compartment of the SOFC. U_{f,H_2} represents the hydrogen utilization in the anode compartment. The partial pressure of oxygen flow in the cathode component is expressed in the form of Eq. (48):

$$P_{O_2} = P \times (1 - U_{f,O_2})\dot{N}_{O_2} \tag{48}$$

where U_{f,O_2} is the oxygen utilization in the cathode compartment. Eqs. (49)–(51) express the fugacity of the reactants and products in the SOFC, derived from the second virial coefficients from the Van der Waals equation of state:

$$f_{H_2} = P_{H_2} \times e^{(0.02665 - \frac{0.2464}{RT}) \times \frac{P_{H_2}}{RT}} \tag{49}$$

$$f_{O_2} = P_{H_2} \times e^{(0.03186 - \frac{1.382}{RT}) \times \frac{P_{O_2}}{RT}} \tag{50}$$

$$f_{H_2} = P_{H_2O} \times e^{(0.03049 - \frac{5.537}{RT}) \times \frac{P_{H_2O}}{RT}} \tag{51}$$

The properties of Solid oxide fuel cell that are used in the model are shown in Table 2.

7.9. Steam methane reformer modeling

Steam methane reforming (SMR) is modeled as an external reformer at 100 bar total pressure and various operating temperatures. The total equilibrium reactions of the catalytic steam methane reformer and water-gas shift are as follows:

Steam methane reforming, Eq. (52):

$$CH_4 + H_2O \Longleftrightarrow CO + 3H_2 \tag{52}$$

Water-Gas shift (WGS) reaction, Eq. (53):

$$CO + H_2O \Longleftrightarrow CO_2 + H_2 \tag{53}$$

8. Results and discussion

The SOFC at high operating pressures has been modeled using the equations presented above. Fig. 5a shows the fuel cell power

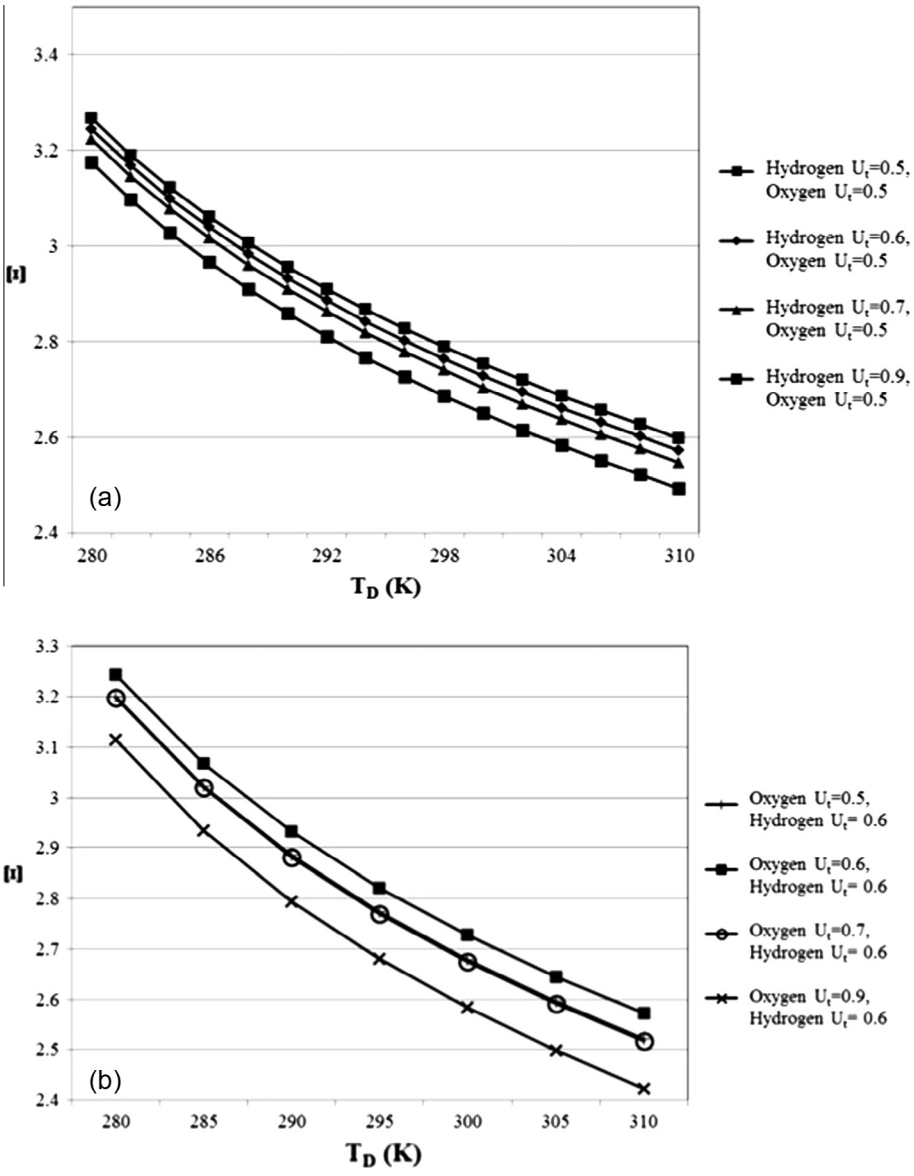

Fig. 10. (a) Non-dimensionalized dissociation front location in the hydrate layer varying with temperature of dissociation at different operating conditions of the hydrogen (Oxygen utilization = 0.5, Case 1). (b) Non-dimensionalized dissociation front location in the hydrate layer varying with temperature of dissociation at different operating conditions of the oxygen (Hydrogen utilization = 0.6, Case 2).

for one cell (it is assumed that there are 18 cells in the fuel cell stack and that each behaves identically) at different levels of oxygen and hydrogen utilization. Each cell operates with a total active area of 50 cm^2 and has been simulated in the deep ocean environment at 100 bar pressure (a region in which gas hydrate formation occurs). The cell power decreases with increasing hydrogen utilization. Increasing hydrogen utilization causes a reduction in the fuel cell voltage mainly because of lower reactant partial pressures at the outlet of the cell. Increases in both hydrogen and oxygen utilization thus result in decreases in hydrogen and oxygen partial pressures at the anode and cathode outlets of the fuel cell and this has an effect on the thermodynamic maximum voltage (Nernst potential) as well as the exchange current density and mass transport losses of the fuel cell. This indicates that obtaining higher power (close to the target power of 1000 W) requires using a fuel cell with lower fuel utilization. However, this will affect the net efficiency of the system, since in that case, more fuel must be provided for steam reformer operation.

Fig. 5b shows the current density of the cell as a function of hydrogen and oxygen utilization at high pressure (100 bar). The manner by which the fuel cell operation is controlled is that of maintaining the cell voltage constant at 0.7 (V). Thus, changing the reactants (hydrogen-rich reformate and oxygen) molar flow rates, results in a change in current density rather than a change in the operating voltage of the cell. Obtaining the same amount of power, therefore, with different fuel utilizations at constant operating voltage (in this case 0.7 (V)), requires a change of current density accordingly. Since the target power is the same in all cases, the current density variation has the same trend as the power variation as a function of the hydrogen and oxygen utilizations.

Fig. 6 shows the effect of high pressure on the stoichiometric concentrations of the effluent gases in the catalytic SMR reactor

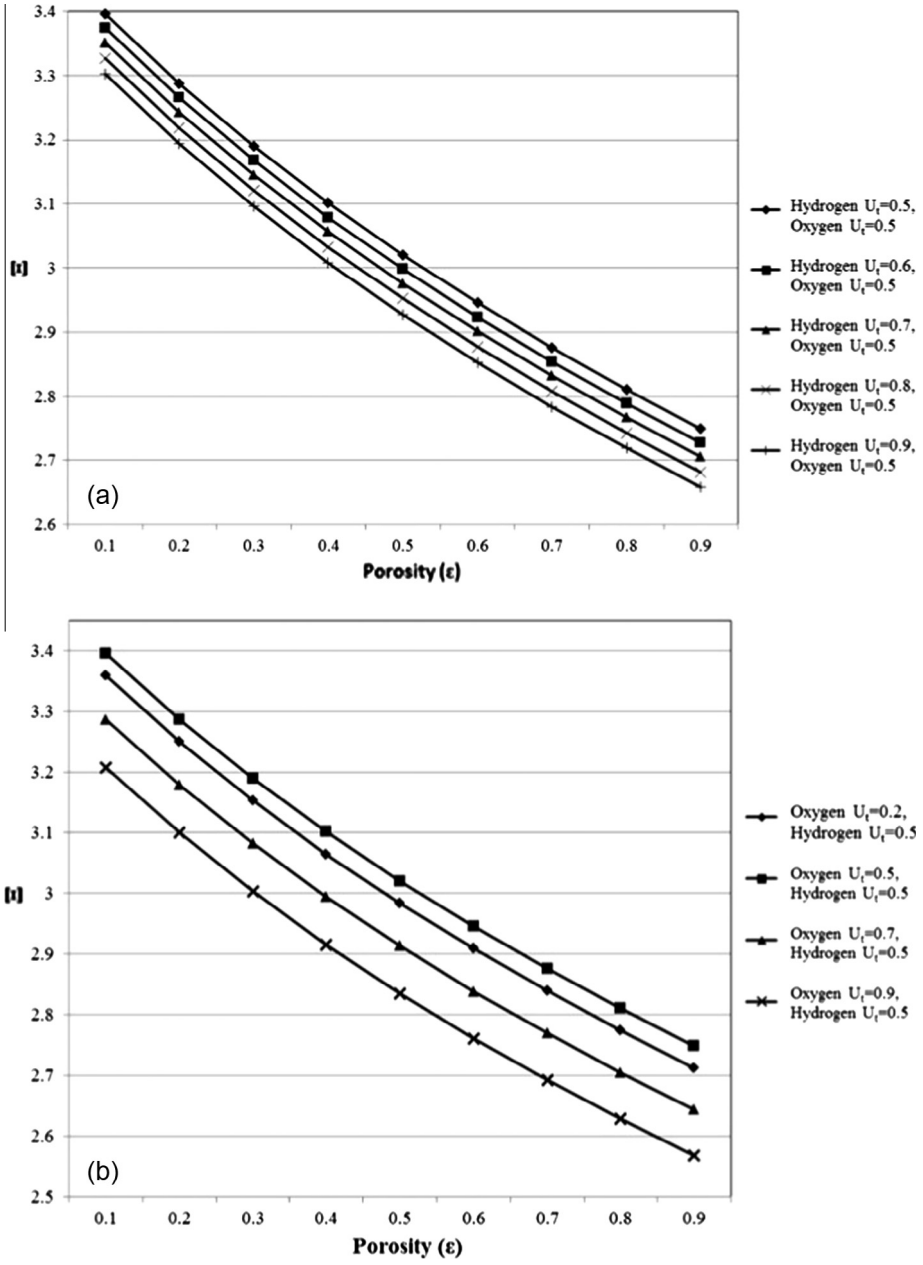

Fig. 11. (a) Non-dimensionalized dissociation front location in the hydrate layer as a function of porosity and hydrogen utilization (Oxygen Utilization = 0.5, Case 1). (b) Non-dimensionalized dissociation front location in the hydrate layer as a function of porosity and hydrogen utilization (Hydrogen Utilization = 0.5, Case 1).

in the temperature range of 750–990 (K) and in the pressure range of 50–130 bar. Concentration of the produced hydrogen in the steam reformer is decreased from 0.3 to 0.2 as pressure is increased from 50 to 130 bar at 1000 K, which shows the negative effect of high pressure operation of SMR on hydrogen production.

Fig. 7a shows that the outlet temperature of the fuel cell effluent gases in the range of hydrogen utilization from 0.5 to 0.9 and oxygen utilization from 0.2 to 0.9. The fuel cell exit temperature increases when hydrogen utilization increases, mainly because of the high electrochemical reaction rate, and lower leftover hydrogen gas in the outlet of the fuel cell. At lower oxygen utilization levels, the temperature increase that results from increased hydrogen utilization is not as significant. The main reason for this effect is the fact that more mass flows through the fuel cell when oxygen utilization is low (cooling the cell).

Fig. 7b shows the temperature of the effluent gases of the heat exchanger as they depend upon oxygen utilization and hydrogen utilization. At low hydrogen utilization ($U_t = 0.2$), the temperature of the heat exchanger (that provides heat to preheat the oxygen) decreases with increasing the oxygen utilization. At high hydrogen utilizations ($U_t = 0.6$ to $U_t = 0.9$), the temperature of the effluent gases of the heat exchanger exhibit both increasing and decreasing trends with oxygen utilization. Fig. 7c illustrates the variation of the temperature of the heat exchanger and the combustor as a function of oxygen utilization for the two different cycle configurations considered. Case 1: heat for the steam methane reformer is provided by burning part of the dissociated methane gas from the hydrate sediment. Case 2: heat for the steam methane reformer is provided by heat exchange with the fuel cell effluent gases. Each case shows increasing temperature with increasing oxygen utilization for low utilizations and decreasing temperature with increasing oxygen utilization for high utilizations. Both combustor and heat exchanger temperatures are always higher for Case 1.

Fig. 8a shows the variation of dissociation front location in the gas hydrate layer after 120 days of system operation, as a function of both reactants utilization in the SOFC system. Generally, the dissociation front location has the same trend as that of the fuel cell exit temperature change with reactant utilizations. Increasing oxygen utilization slows down the dissociation front development rate at lower hydrogen utilization because it reduces mass flow rate.

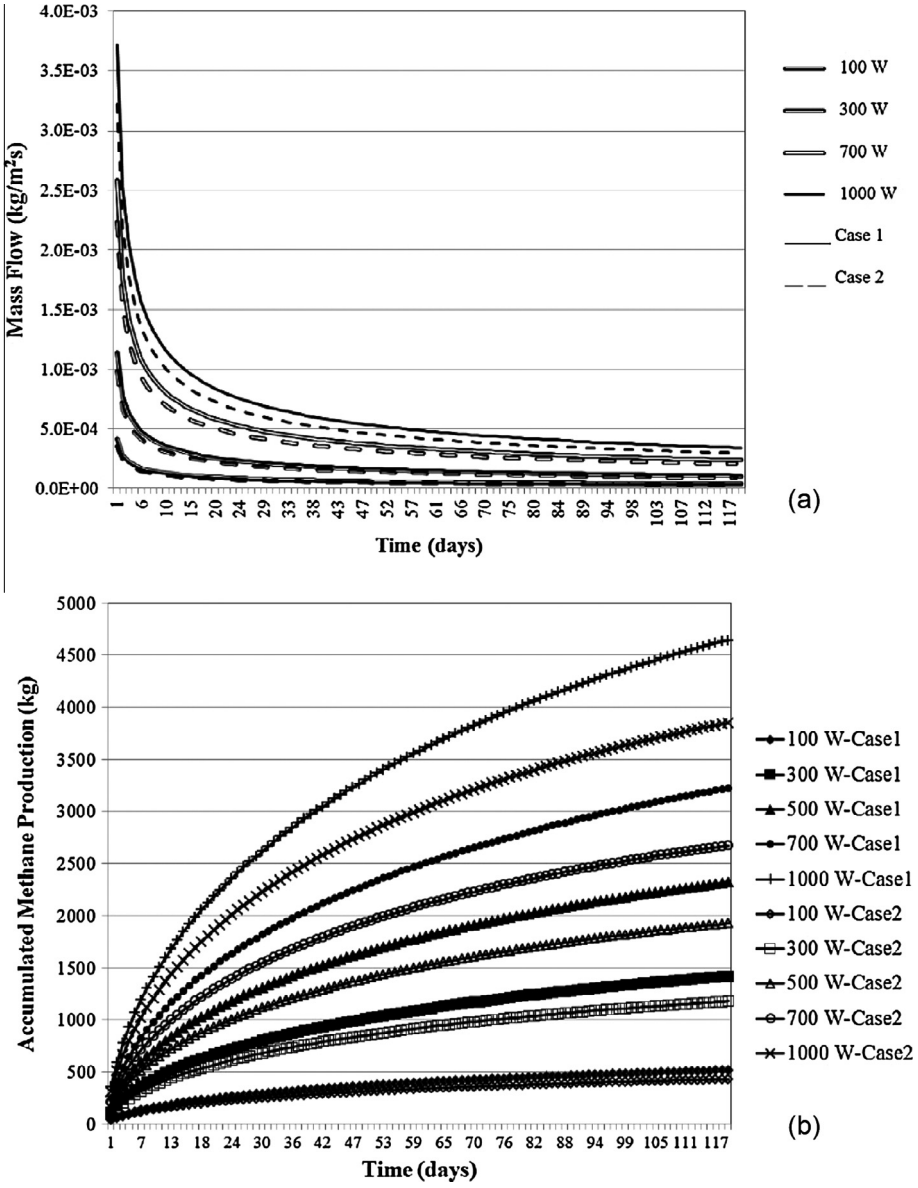

Fig. 12. (a) Methane gas mass production over time (O_2 utilization = 0.5, H_2 utilization = 0.7). (b) Accumulated gas production during time (O_2 utilization = 0.5, H_2 utilization = 0.7).

Fig. 8b shows the dissociation front location variation during time for different porosities of the hydrate layer. In layers with high porosity, the chance for more hydrate dissociation in the saturated layer is greater. Hence, the dissociation front moves slower than in the layer with less porosity, since there is more heat required for dissociation to decompose the layer.

Fig. 9 illustrates the temperature rise development in the hydrate sediment for two different hydrogen utilizations (0.62 and 0.9), while the oxygen utilization is held constant at 0.5. The temperature profile depends upon several parameters of hydrate layer including permeability, temperature of dissociation, pressure of dissociation, thermal conductivity of two zones and other factors. The values used in these computations are shown in Table 1. The trends for the two cases show a development of dissociation that is similar with deeper penetration into the sediment for the higher temperature hydrogen utilization case of 0.62.

Fig. 10 demonstrates the non-dimensional dissociation front location in the hydrate layer as it depends upon the temperature of dissociation for different utilizations of hydrogen and oxygen. The value of the Ξ parameter drops as the temperature of dissociation increases. Because of greater temperature of dissociation, there is less temperature difference between the thermal stimulation source (SOFC) and the cold dissociation front. Therefore, the heat flux is less effective and the hydrate front moves slower than the case with lower temperature of dissociation. In addition, at oxygen utilization level of 0.2, the heat exchanger temperature drops as hydrogen utilization increases. Hence, the dissociation front moves slower than for the case of lower hydrogen utilization.

Fig. 11 illustrates the non-dimensional dissociation front location in the hydrate layer as a function of porosity and the SOFC performance parameters. It can be seen that the hydrogen utilization change has a lesser effect on the Ξ parameter than the oxygen utilization does. Increasing the oxygen utilization from 0.2 to 0.9 reduces the Ξ parameter by about 0.2. However, Increasing the hydrogen utilization from 0.5 to 0.9 will decrease the parameter by only 0.1.

Fig. 12a shows the methane mass flow production for 120 days and different power loads of the SOFC for the two different cycle cases considered. In system case 1, it is obvious that the temperature of the fuel cell effluent gases is higher than that of system case 2, so that the mass production of methane is higher in this case because of a higher rate of the dissociation process caused by higher temperatures.

The accumulated mass production of the methane gas over a 120 days period is shown in Fig. 12b for different power loads and for the two cycle cases considered. The mass production rate

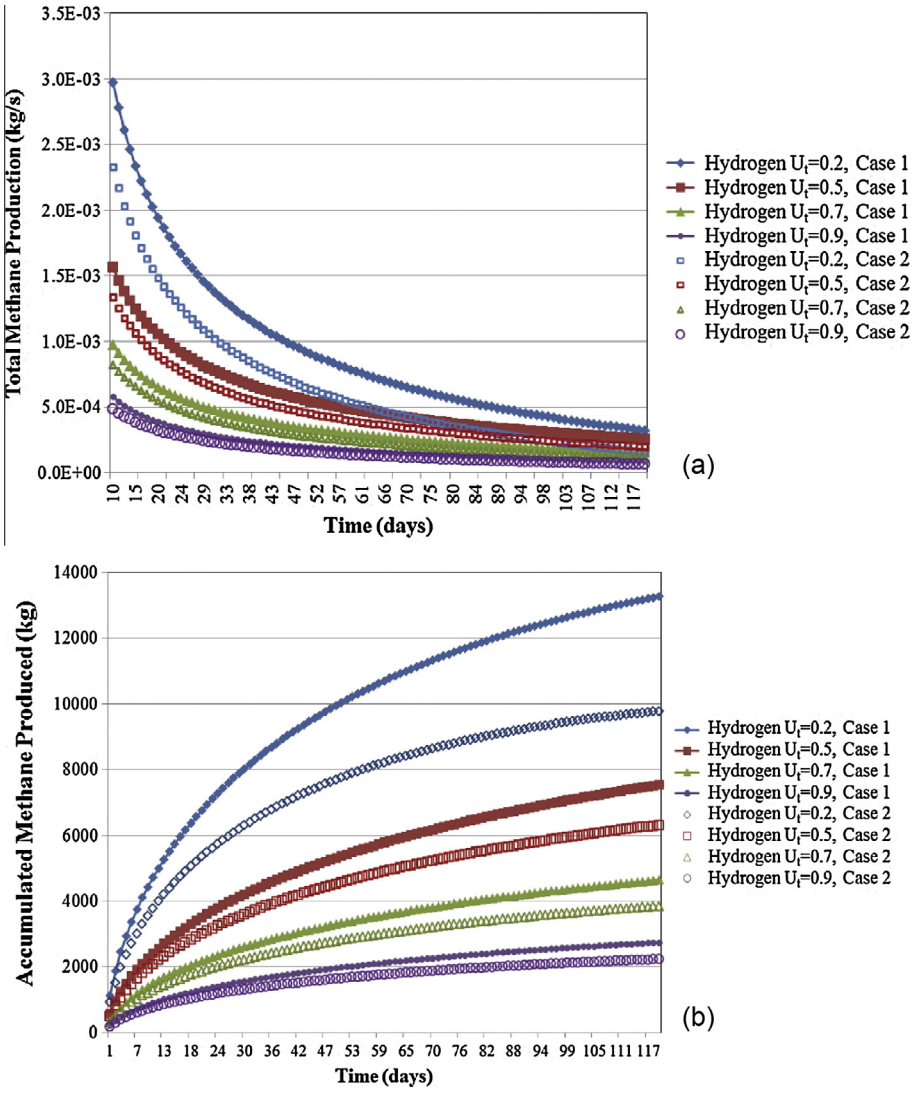

Fig. 13. (a) Total methane production for different operations of fuel cell (H_2 utilizations), Oxygen utilization = 0.5, Produced power = 1000 W. (b) Accumulated methane produced over a period of time for different operations of fuel cell (O_2 utilization = 0.5), Produced power = 1000 W.

decreases because of the velocity of the dissociation front decreases during the entire period of operation. Fig. 13a shows the total methane gas production for the entire 120 days for different levels of SOFC system hydrogen utilizations and two cases of system operation. The amount of methane required for SMR operation is included in these analyses.

Fig. 13b illustrates that the accumulated methane production in a time period of 120 days depends upon the SOFC hydrogen utilization used. As hydrogen utilization increases the amount of accumulated methane decreases primarily because the quality of the heat available from the SOFC decreases.

Fig. 14a shows accumulated methane gas production after 120 days operation of the integrated SOFC hydrate bed system versus power generation and SOFC hydrogen utilizations in the range of 0.2–0.9, and for the two cycle cases considered. Note that Case 1 produces more methane than Case 2 for all conditions considered and that more methane is produced when more power is produced. Fig. 14b illustrates the accumulated methane gas production after 120 days operation of SOFC system versus power generation and SOFC oxygen utilizations in the range of 0.2–0.8, and for the two cycle cases considered. Note that oxygen utilization does not as significantly affect accumulated methane levels as hydrogen utilization does.

Fig. 15 shows the maximum amount of power that the SOFC system can generate combined with the depressurization method for different values of SOFC hydrogen utilization. A high hydrogen utilization fuel cell generates less power than a low hydrogen utilization one. However, the system consumes a lesser amount of methane gas to be converted into hydrogen in the steam reformer. Fig. 15 also demonstrates that the net efficiency of fuel cell system

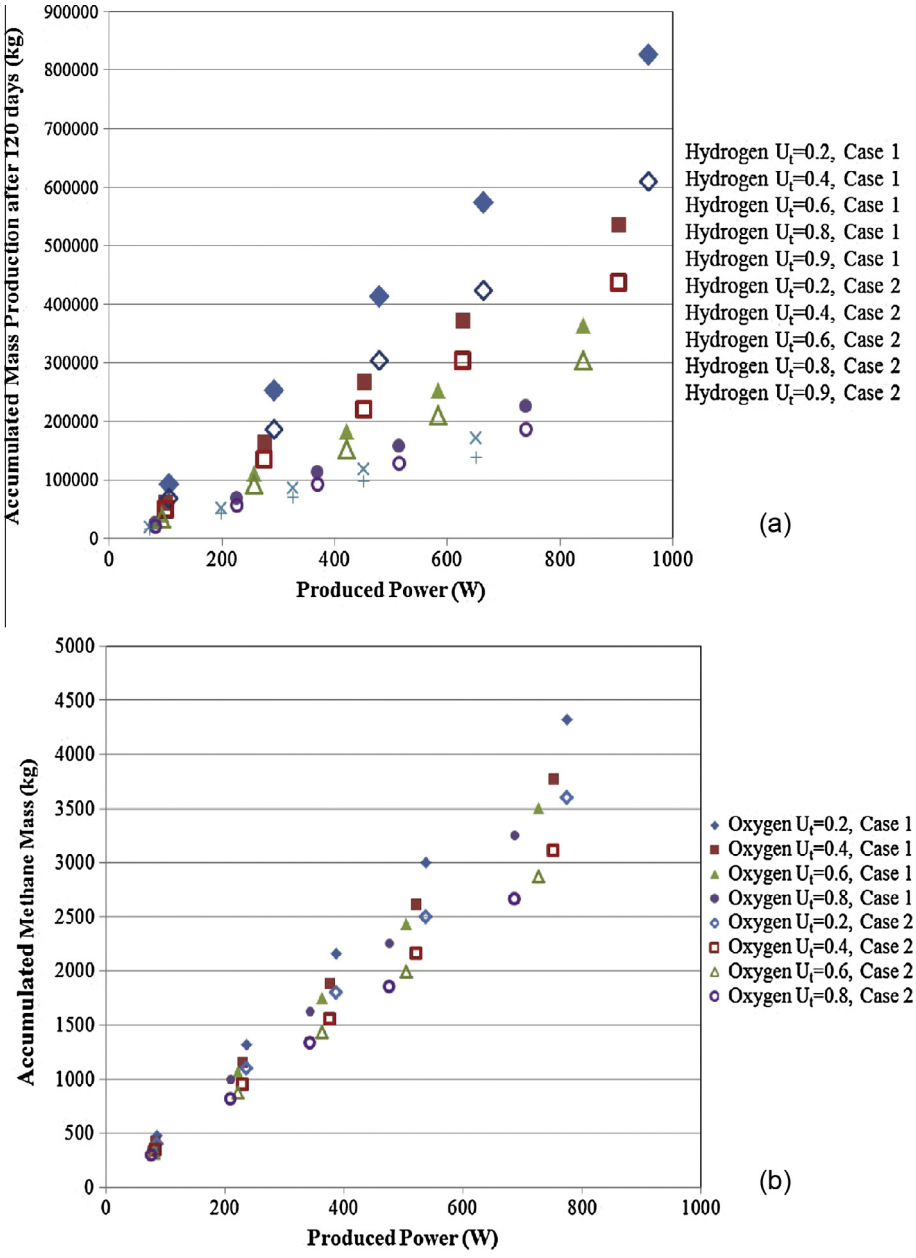

Fig. 14. (a) Accumulated production of methane after 120 days versus the produced power of fuel cell for different operating conditions of the fuel cell (Constant O_2 utilization = 0.5). (b) Accumulated production of methane after 120 days versus the produced power of fuel cell for different operations of fuel cell (Constant H_2 utilization = 0.8).

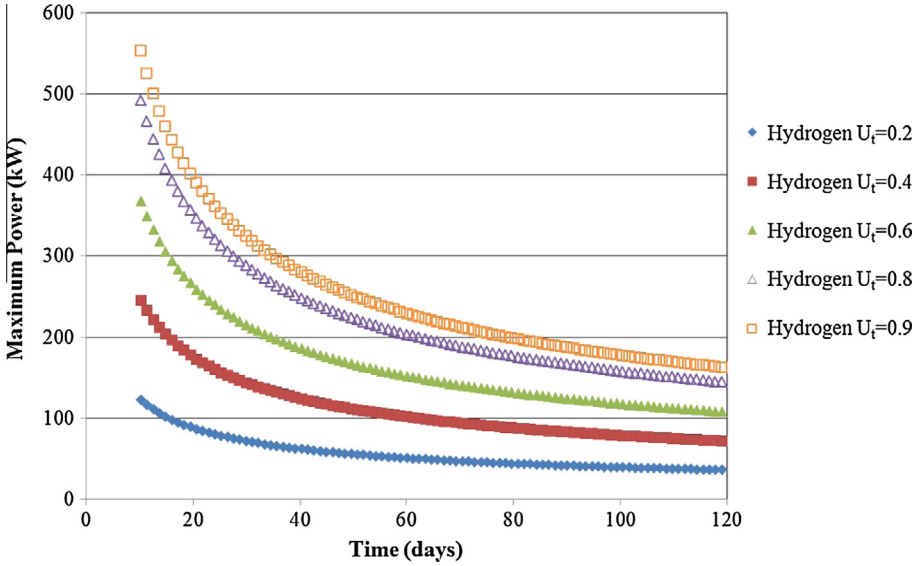

Fig. 15. Maximum power generation by SOFC based on depressurized hydrate reservoir at constant hydrogen utilization = 0.6 and P_W = 4 MPa.

for higher fuel utilization is larger than that of the fuel cell system with low utilization, since it consumes less of the produced methane in the reformer.

9. Conclusions

In this study, thermodynamics, energy and mass balance principles have been used to show that a solid oxide fuel cell system (SOFC) can operate steadily for at least 120 days at the high pressure deep ocean environment of a methane hydrate bed. Integrated simulations of the hydrate bed coupled to the heat release of the SOFC were accomplished. Accessible net amounts of methane gas production were realized in the simulations of the deep ocean environment. Two different system operating scenarios are simulated and compared, which primarily address the heat provision for the steam methane reformer (SMR) of the SOFC system. The first system operating scenario involves: providing the endothermic energy by burning part of the dissociated methane from the hydrate sediment. The second system scenario involves providing the endothermic energy from heat exchange with effluent gases of the fuel cell. These two system scenarios are compared, with respect to the net amount of methane gas production achieved in each case. The system analyses show that larger amounts of methane can be produced for the case where heat is provided by burning a portion of the dissociated methane gas.

In addition, the study evaluates different operational parameters of solid oxide fuel cell (e.g., reactant utilization), for the methane gas production from a hydrate layer. This study showed that despite the fact that a low reactant utilization fuel cell produces more power than the higher utilization fuel cell, the integrated system net efficiency is lower than the high fuel utilization SOFC system, due to the fact that less methane gas is needed in the steam methane reformer. The study also investigated the maximum power that could be generated as combined with the depressurization approach for 4 MPa well pressure.

Appendix A

Under the assumptions that were mentioned in the model description section, the similarity solution to the system of equations has been found as [22]:

$$\frac{T_I - T_0}{T_D - T_0} = \frac{erf(C_1\Pi + C_2) - erfC_2}{erf(C_1\Xi + C_2) - erfC_2} \tag{A1}$$

$$\frac{T_{II} - T_i}{T_D - T_i} = \frac{erfc(\Pi)}{erfc(\Xi)} \tag{A2}$$

$$C_1 \frac{k_I(T_0 - T_D)}{k_{II}(T_D - T_i)} \frac{\exp\left[-(C_1\Xi + C_2)^2\right]}{erf(C_1\Xi + C_2) - erf(b)} - \frac{\exp(-\Xi^2)}{erfc(\Xi)} = \sqrt{\pi}\varepsilon \frac{\rho_{hydrate}}{\rho_{II}} St\Xi \tag{A3}$$

$$C_1 = \left(\frac{\alpha_{II}}{\alpha_I}\right)^{\frac{1}{2}} \tag{A4}$$

$$C_2 = C_{p,g} \frac{\omega\varepsilon\rho_{hydrate}\alpha_{II}}{C_1 k_1}\Xi \tag{A5}$$

The Stefan number (ST) has been derived to be:

$$St = \frac{\Delta H}{C_{p_{II}}(T_D - T_i)} \tag{A6}$$

Appendix B

The distribution of pressure in the layer is described by Stefan's one dimensional melting problem [71]:

$$\frac{2\varepsilon_n\mu}{k_n}\frac{\partial P_n}{\partial t} = \frac{\partial P_n^2}{\partial x^2} \tag{B1}$$

where

$$\varepsilon_1 = (1 - \tau)\varepsilon \tag{B2}$$

$$\varepsilon_2 = (1 - \beta)\varepsilon \tag{B3}$$

ε is the porosity of the one dimensional hydrate layer. ε_1 and ε_2 are the amount of free gas and hydrate layer. μ is the viscosity of the gas in zones 1 or 2. k_1 and k_2 are the phase permeabilites of gas in zone 1 or 2. P_1 and P_2 are the pressure distributions in zones 1 and 2 respectively. τ is the water content of the porous media. β

is the methane hydrate saturation in the one dimensional hydrate layer.

Index n = 1 is associated with the region $0 < x < X(t)$, and the index n = 2 is associated with the region $X(t) < x < \infty$. $X(t)$ is the position of dissociation front which separates zones 1 and 2.

$P_D(T_D)$ expresses the equilibrium relation between the pressure and the temperature of hydrate decomposition T_D at the dissociation front. This relationship could be expressed in the form of:

$$\log P_D = a(T_D - T_0) + b(T_D - T_0)^2 + c \tag{B4}$$

P_D is in Pa.

a, b, c are the experimental constants depending on the hydrate structure and pressure and temperature variation. a, b and c have been found to be [74]:

$$a = 0.0342\frac{1}{K},\ b = 0.0005\frac{1}{K^2},\ c = 6.4804 \tag{B5}$$

$$T_1 = T_D + A_1\delta[erf\ \xi_1 - erf\kappa_1 - \left(\frac{\eta}{\delta}B_1 - 1\right)(\Phi_1(\kappa_1) - \Phi_1(\xi_1)) \tag{B6}$$

$$T_2 = T_i + A_2\delta\left[erfc\ \xi_2 - \Phi_2(\xi_2) - \frac{\eta}{\delta}B_2\Phi_2(\xi_2)\right] \tag{B7}$$

Using Linearization suggested by Ji et al. [74]:

$$\frac{\partial P_1^2}{\partial t} \approx 2P_w\frac{\partial P_1}{\partial t},\quad \frac{\partial P_2^2}{\partial t^2} \approx 2P_i\frac{\partial P_2}{\partial t} \tag{B8}$$

$$\frac{\partial P_n^2}{\partial t^2} \approx \Lambda_n\frac{\partial^2 P_n}{\partial x^2} \quad n = 1,2 \tag{B9}$$

$$\Lambda_1 = \frac{k_1 P_g}{\varepsilon(1-\tau)\mu},\ \Lambda_2 = \frac{k_2 P_i}{\varepsilon(1-\beta)\mu} \tag{B10}$$

$$P_1^2 = P_w^2 - \left(P_w^2 - P_D^2\right)\frac{erf\xi_1}{erf\kappa_1} \tag{B11}$$

$$P_2^2 = P_i^2 - \left(P_i^2 - P_D^2\right)\frac{erf\hat{a}\text{¡}\ \xi_2}{erf\kappa_2} \tag{B12}$$

where

$$\xi_n = \frac{x}{2\sqrt{\Lambda_n t}},\ \kappa_n = \sqrt{\frac{\sigma}{4\Lambda_n}} \tag{B13}$$

$$erf\xi = \frac{2}{\sqrt{\pi}\int_0^{\xi} e^{-\eta^2}\ d\eta} \tag{B14}$$

$$\Phi_1(\tau_0) = \frac{2}{\sqrt{\pi}}\int_0^{\tau_0}\frac{ve^{-v^2}}{v + C_1e^{-v^2}}\ dv \tag{B15}$$

$$\Phi_2(\tau_0) = \frac{2}{\sqrt{\pi}}\int_{\tau_0}^{\infty}\frac{ve^{-v^2}}{v + C_2e^{-v^2}}\ dv \tag{B16}$$

$$A_1 = \frac{2}{erf\xi_1}\frac{P_D^2 - P_w^2}{P_w} \tag{B17}$$

$$A_2 = \frac{2}{erfc\xi_2}\frac{P_i^2 - P_D^2}{P_i} \tag{B18}$$

$$B_1 = \frac{P_w^2\varepsilon_1 c_{0,v}}{4P_0c_1},\ B_2 = \frac{P_i^2\varepsilon_2 c_{0,v}}{4P_0c_2} \tag{B19}$$

$$C_1 = \frac{P_D^2 - P_w^2}{P_w}\frac{c_v}{c_1}\frac{1}{2\sqrt{\pi}erf\xi_1}\frac{k_1}{\mu\Lambda_1} \tag{B20}$$

$$C_2 = \frac{P_i^2 - P_D^2}{P_i}\frac{c_v}{c_2}\frac{1}{2\sqrt{\pi}erf\xi_2}\frac{k_2}{\mu\Lambda_2} \tag{B21}$$

References

[1] McIver RD. Gas hydrates. In: Meyer RF, Olson JC, editors. Long-term energy resources, vol. 1. Boston (MA): Pitman; 1981. p. 713–26.
[2] Trofimuk AA, Cherskiy NV, Tsarev VP. The gas-hydrate sources of hydrocarbons. Priroda 1979;1:18–27.
[3] Makogon YF. Perspectives for the oil and gas industry in the world. Gazovaya Promishlennost (Gas Industry), no. 8. Moscow; 1984.
[4] Makogon YF. Razrabotka gazogidratnoy zalezhi (Production from natural gas hydrate deposits), vol. 10. Gazovaya Promishlennost; 1984. p. 24–6.
[5] NETL. Energy resource potential of methane hydrate, an introduction to the science and energy potential of a unique resource. National Energy Technology Laboratory; 2011.
[6] Hammerschmidt EG. Formation of gas hydrates in natural gas transmission lines. Ind Eng Chem 1934;26(8):851–5.
[7] Robinson DB, Ng HJ. Hydrocarbon processing 95; December 1976.
[8] Schoderbek D. ConocoPhillips gas hydrate production test, semi-annual progress report, First Half. DOE Award No: DE-NT00065532012; 2012.
[9] Tishchenko Pavel et al. Calculation of the stability and solubility of methane hydrate in seawater. Chem Geol 2005;219(1):37–52.
[10] Duan Zhenhao, Møller Nancy, Weare John H. An equation of state for the CH_4–CO_2–H_2O system: I. Pure systems from 0 to 1000 °C and 0 to 8000 bar. Geochim Cosmochim Acta 1992;56(7):2605–17.
[11] Duan Zhenhao et al. The prediction of methane solubility in natural waters to high ionic strength from 0 to 250 °C and from 0 to 1600 bar. Geochim Cosmochim Acta 1992;56(4):1451–60.
[12] Duan Zhenhao, Mao Shide. A thermodynamic model for calculating methane solubility, density and gas phase composition of methane-bearing aqueous fluids from 273 to 523 K and from 1 to 2000 bar. Geochim Cosmochim Acta 2006;70(13):3369–86.
[13] Hyndman RD et al. Geophysical studies of marine gas hydrate in northern Cascadia. Nat Gas Hyd 2001:273–95.
[14] Collett TS et al. Detailed evaluation of gas hydrate reservoir properties using JAPEX/JNOC/GSC Mallik 2L-38 gas hydrate research well downhole well-log displays. Bull-Geol Surv Canada 1999:295–312.
[15] Handa Y Paul. Effect of hydrostatic pressure and salinity on the stability of gas hydrates. J Phys Chem 1990;94(6):2652–7.
[16] Sloan ED. Clathrate hydrates of natural gases. New York: Marcel Dekker Inc; 1998.
[17] Pfefferle WC. Method of natural gas production. US Patent No 6,973,968 13; 2005.
[18] Tsimpanogiannis Ioannis N, Lichtner Peter C. Parametric study of methane hydrate dissociation in oceanic sediments driven by thermal stimulation. J Petrol Sci Eng 2007;56(1):165–75.
[19] Chatterjee S, Dickens GR, Bhatnagar G, Chapman WG, Dugan B, Snyder GT, et al. Pore water sulfate, alkalinity, and carbon isotope profiles in shallow sediment above marine gas hydrate systems: a numerical modeling perspective. J Geophys Res-Solid Earth 2011;116.
[20] Holder GD et al. A thermodynamic evaluation of thermal recovery of gas from hydrates in the earth (includes associated papers 11863 and 11924). J Petrol Technol 1982;34(5):1127–32.
[21] Bayles GA et al. A steam cycling model for gas production from a hydrate reservoir. Chem Eng Commun 1986;47(4-6):225–45.
[22] Selim MS, Sloan ED. Heat and mass transfer during the dissociation of hydrates in porous media. AIChE J 1989;35(6):1049–52.
[23] Selim MS, Sloan ED. Hydrate dissociation in sediment. SPE Reserv Eng 1990;5 (2):245–51.
[24] Ullerich JW, Selim MS, Sloan ED. Theory and measurement of hydrate dissociation. AIChE J 1987;33(5):747–52.
[25] Tsypkin GG. Gas hydrate dissociation regimes in highly permeable beds. J Eng Phys Thermophys 1992;63(6):1221–7.
[26] Islam MR. A new recovery technique for gas production from Alaskan gas hydrates. J Petrol Sci Eng 1994;11(4):267–81.
[27] Castaldi Marco J, Zhou Yue, Yegulalp Tuncel M. Down-hole combustion method for gas production from methane hydrates. J Petrol Sci Eng 2007;56 (1):176–85.
[28] McGuire Patrick L. Methane hydrate gas production by thermal stimulation. No. LA-UR-81-645; CONF-810317-1. NM (USA): Los Alamos Scientific Lab.; 1981.
[29] Goodman Theodore R. The heat-balance integral and its application to problems involving a change of phase. Trans ASME 1958;80(2):335–42.
[30] Li Xiao-Sen et al. Experimental investigation into methane hydrate production during three-dimensional thermal huff and puff. Appl Energy 2012;94:48–57.
[31] Wang Yi et al. Experimental investigation into methane hydrate production during three-dimensional thermal stimulation with five-spot well system. Appl Energy 2013;110:90–7.
[32] Torres ME et al. Fluid and chemical fluxes in and out of sediments hosting methane hydrate deposits on Hydrate Ridge, OR, I: Hydrological provinces. Earth Planet Sci Lett 2002;201(3):525–40.

[33] Makogan YF, Holditch SA, Makogan TY. Russian field illustrates gas–hydrate production. Oil Gas J 2005;103:43–7.
[34] Yousif MH, Sloan ED. Experimental investigation of hydrate formation and dissociation in consolidated porous media. SPE Reserv Eng 1991;6:452–8.
[35] Yousif MH, Abass HH, Selim MS, Sloan ED. Experimental and theoretical investigation of methane–gas–hydrate dissociation in porous media. SPE Reserv Eng 1991;6:69–76.
[36] Goel Naval, Wiggins Michael, Shah Subhash. Analytical modeling of gas recovery from in situ hydrates dissociation. J Petrol Sci Eng 2001;29 (2):115–27.
[37] Li Xiao-Sen et al. Experimental investigation into gas production from methane hydrate in sediment by depressurization in a novel pilot-scale hydrate simulator. Appl Energy 2012;93:722–32.
[38] Li Bo et al. Depressurization induced gas production from hydrate deposits with low gas saturation in a pilot-scale hydrate simulator. Appl Energy 2014;129:274–86.
[39] Wang Yi, Feng Jingchun, Li Xiaosen, Zhang Yu. Analytic modeling and large-scale experimental study of mass and heat transfer during hydrate dissociation in sediment with different dissociation methods. Energy 2015;90:1931–48.
[40] Wang Yi, Feng Jingchun, Li Xiaosen, Zhang Yu, Li Gang. Large scale experimental evaluation to methane hydrate dissociation below quadruple point in sandy sediment. Appl Energy 2016;162:372–81.
[41] Song Yongchen et al. Evaluation of gas production from methane hydrates using depressurization, thermal stimulation and combined methods. Appl Energy 2015;145:265–77.
[42] Alp D, Parlaktuna M, Moridis GJ. Gas production by depressurization from hypothetical Class 1G and Class 1W hydrate reservoirs. Energy Convers Manage 2007;48:1864–79.
[43] Gupta A, Kneafsey TJ, Moridis GJ, Seol Y, Kowalsky MB, Sloan ED. Composite thermal conductivity in a large heterogeneous porous methane hydrate sample. J Phys Chem B 2006;110:16384–92.
[44] Moridis George J et al. Numerical studies of gas production from several CH_4 hydrate zones at the Mallik site, Mackenzie Delta, Canada. J Petrol Sci Eng 2004;43(3):219–38.
[45] Santamarina JC, Tsouris C. Methane recovery from hydrate-bearing sediments, final scientific/technical report. DOE Award No.: DE-FC26-06NT42963. Georgia Institute of Technology; 2011.
[46] Bhangale A, Zhu T, McGrail B, White M. A model to predict hydrate equilibrium and hydrate saturation inside porous media including mixed CH_4–CO_2 hydrates. In: Proceedings of the SPE-improved oil recovery symposium; 2006 [paper SPE 99759].
[47] Phale H, Zhu T, White M, McGrail B. Simulation study on injection of CO_2-microemulsion for methane recovery from gas-hydrate reservoirs. In: Proceedings of the SPE-improved oil recovery symposium; 2006 [paper SPE 100541].
[48] Sawyer Wilbur H. Comparative physiology and pharmacology of the neurochypophysis. Recent Prog Horm Res 1961;17:437.
[49] Khataniar Santanu et al. Modeling and economic analysis of gas production from hydrates by depressurization method. Can J Chem Eng 2002;80 (1):135–43.
[50] Park Sung Ku et al. An integrated power generation system combining solid oxide fuel cell and oxy-fuel combustion for high performance and CO_2 capture. Appl Energy 2011;88(4):1187–96.
[51] Park Sung Ku, Ahn Ji-Ho, Kim Tong Seop. Performance evaluation of integrated gasification solid oxide fuel cell/gas turbine systems including carbon dioxide capture. Appl Energy 2011;889:2976–87.
[52] Santin Marco, Traverso Alberto, Magistri Loredana. Liquid fuel utilization in SOFC hybrid systems. Appl Energy 2009;86(10):2204–12.
[53] Laguna-Bercero MA. Recent advances in high temperature electrolysis using solid oxide fuel cells: a review. J Power Sources 2012;203:4–16.
[54] Millet P, Ngameni R, Grigoriev SA, Mbemba N, Brisset F, Ranjbari A, et al. PEM water electrolyzers: from electrocatalysis to stack development. Int J Hydrogen Energy 2010;35:5043–52.
[55] Roberts RA, Brouwer J. Dynamic simulation of a pressurized 220 kW solid oxide fuel-cell-gas-turbine hybrid system: modeled performance compared to measured results. J Fuel Cell Sci Technol 2006;3:18–25.
[56] Roberts R, Brouwer J, Jabbari F, Junker T, Ghezel-Ayagh H. Control design of an atmospheric solid oxide fuel cell/gas turbine hybrid system: variable versus fixed speed gas turbine operation. J Power Sources 2006;161:484–91.
[57] Mueller F, Brouwer J, Jabbari F, Samuelsen S. Dynamic simulation of an integrated solid oxide fuel cell system including current-based fuel flow control. J Fuel Cell Sci Technol 2006;3:144–54.
[58] Costamagna P, Selimovic A, Del Borghi M, Agnew G. Electrochemical model of the integrated planar solid oxide fuel cell (IP-SOFC). Chem Eng J 2004;102:61–9.
[59] Selamet OF, Acar MC, Mat MD, Kaplan Y. Effects of operating parameters on the performance of a high-pressure proton exchange membrane electrolyzer. Int J Energy Res 2013;37:457–67.
[60] Myles TD, Nelson GJ, Peracchio AA, Roy RJ, Murach BL, Adamson GA, et al. Species transport in a high-pressure oxygen-generating proton-exchange membrane electrolyzer. Int J Hydrogen Energy 2012;37:12451–63.
[61] Marini S, Salvi P, Nelli P, Pesenti R, Villa M, Berrettoni M, et al. Advanced alkaline water electrolysis. Electrochim Acta 2012;82:384–91.
[62] Williams MC, Strakey J, Sudoval W. U.S. DOE fossil energy fuel cells program. J Power Sources 2006;159:1241–7.
[63] Williams MC, Strakey JP, Surdoval WA. The U.S. Department of Energy, Office of Fossil Energy Stationary Fuel Cell Program. J Power Sources 2005;143:191–6.
[64] Williams MC, Strakey JP, Singhal SC. U.S. distributed generation fuel cell program. J Power Sources 2004;131:79–85.
[65] Savaniu CD, Irvine JTS. Reduction studies and evaluation of surface modified A-site deficient La-doped $SrTiO_3$ as anode material for IT-SOFCs. J Mater Chem 2009;19:8119–28.
[66] Luo H, Efimov K, Jiang H, Feldhoff A, Wang H, Caro J. CO_2-stable and cobalt-free dual-phase membrane for oxygen separation. Angew Chem Int Ed 2011;50:759–63.
[67] Pine T, Do A-TV, Zhao L, Brouwer J. Operation of a novel dry hydrocarbon tolerant intermediate temperature solid oxide fuel cell. ASME conference proceedings 2009. p. 761–6.
[68] Zhao HL, Gao F, Li X, Zhang CJ, Zhao YQ. Electrical properties of yttrium doped strontium titanate with A-site deficiency as potential anode materials for solid oxide fuel cells. Solid State Ionics 2009;180:193–7.
[69] Goodenough JB, Huang YH. Alternative anode materials for solid oxide fuel cells. J Power Sources 2007;173:1–10.
[70] Bird R Byron, Stewart Warren E, Lightfoot Edwin N. Transport phenomena. John Wiley & Sons; 2007.
[71] Makogon IF. Hydrates of hydrocarbons. Pennwell Books; 1997.
[72] Bondarev EA, et al. Mechanics of hydrate formation in gas flows; 1976.
[73] Verigin NN, Khabibullin IL, Khalikov GA. Linear problem of gas hydrate decomposition in a porous medium. Izv Akad Nauk SSSR, Mekh Zhidk Gaza 1980;1:174.
[74] Ji Chuang, Ahmadi Goodarz, Smith Duane H. Natural gas production from hydrate decomposition by depressurization. Chem Eng Sci 2001;56 (20):5801–14.